

**ADHESIVE JOINT ANALYSES USING ANSYS CZM MODELING
OF A PREFABRICATED HYBRID CONCRETE-GFRP-CFRP UNIT**

by

Maksim Kabaluk

A Thesis Submitted to the Faculty of
College of Engineering and Computer Science
In Partial Fulfillment of the Requirements for the Degree of
Master of Science

Florida Atlantic University

Boca Raton, FL

May 2019

ProQuest Number: 13862837

All rights reserved

INFORMATION TO ALL USERS

The quality of this reproduction is dependent upon the quality of the copy submitted.

In the unlikely event that the author did not send a complete manuscript and there are missing pages, these will be noted. Also, if material had to be removed, a note will indicate the deletion.



ProQuest 13862837

Published by ProQuest LLC (2019). Copyright of the Dissertation is held by the Author.

All rights reserved.

This work is protected against unauthorized copying under Title 17, United States Code
Microform Edition © ProQuest LLC.

ProQuest LLC.
789 East Eisenhower Parkway
P.O. Box 1346
Ann Arbor, MI 48106 – 1346

Copyright 2019 by Maksim Kabaluk

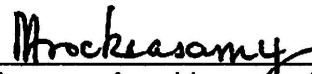
**ADHESIVE JOINT ANALYSES USING ANSYS CZM MODELING OF A
PREFABRICATED HYBRID CONCRETE-GFRP-CFRP UNIT**

by


Maksim Kabaluk

This thesis was prepared under the direction of the candidate's thesis advisor, Dr. Madasamy Arockiasamy, Department of Civil, Environmental, and Geomatics Engineering, and has been approved by the members of his supervisory committee. It was submitted to the faculty of the College of Engineering and Computer Science and was accepted in partial fulfillment of the requirements for the degree of Master of Science.


SUPERVISORY COMMITTEE:



Madasamy Arockiasamy, Ph.D.
Thesis Advisor



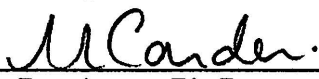
Yan Yong, Ph.D.




Khaled Sobhan, Ph.D.



Yan Yong, Ph.D.
Chair, Department of Civil,
Environmental, and Geomatics
Engineering



Stella Batalama, Ph.D.
Dean, College of Engineering
and Computer Science



Khaled Sobhan, Ph.D.
Interim Dean, Graduate College

April 18, 2019
Date

ACKNOWLEDGEMENTS

I wish to express sincere gratitude to my thesis advisor Professor Dr. Madasamy Arockiasamy for his continuous support, patience, motivation, and immense knowledge he has shared with me during research for this manuscript. The door to Professor Arockiasamy's office was always open. As a great mentor, whenever I had an issue, or a question Professor Arockiasamy was reliably available to help me. Occasionally, he would steer me in the right direction whenever I needed it while allowing this paper to be my own work. I would also like to acknowledge and thank to Professor and Interim Dean of Graduate College Dr. Khaled Sobhan and Professor and Department Chair Dr. Yan Yong as the additional readers of this manuscript, and I am grateful to their valuable comments.

I would like to thank to the staff of the Florida Atlantic University library at Boca Raton campus. They provided me with necessary technical support, which allowed me to obtain documentation required for this thesis.

A special gratitude goes to S&F Engineers for allowing me to conduct my research and work par-time. I am grateful to be a part of their engineering team. I am appreciative to the Principals of S&F Engineers, Sri Sritharan and Donata Williams, for their support and for giving me a chance to prove myself. Thank you, for the continues professional mentoring.

I am grateful to my family that is always there for me during my highs and lows. Special thank is to my wife/best friend who is consistently providing me with moral

and emotional support in my life. Thank you for your constant care and for your understanding. I am also grateful to my friend who supported me along the way.

ABSTRACT

Autor: Maksim Kabaluk
Title: Adhesive Joint Analyses Using ANSYS CZM Modeling of a Prefabricated Hybrid Concrete-GFRP-CFRP Unit
Institution: Florida Atlantic University
Thesis Advisor: Dr. M. Arockiasamy, P.E.
Degree: Master of Science
Year: 2019

The present study reviews applications of FRP materials joined by structural adhesives in civil engineering. FE analysis with mix-mode cohesive zone material model (CZM) was used to analyze stresses induced in two structural adhesives joining dissimilar materials (concrete-GFRP-CFRP) of the hybrid-composite unit. The predicted failure loads, displacements and deformation by the 3-D non-linear FE analysis in the present study are in good agreement with the experimental results of the hybrid-composite unit reported by Deskovic et al. (1995). The contact analysis revealed a complex 3-D state of stress in the bondlines of both structural adhesives. It is concluded that higher joint strength is expected when a ductile adhesive is used.

**ADHESIVE JOINT ANALYSES USING ANSYS CZM MODELING
OF A PREFABRICATED HYBRID CONCRETE-GFRP-CFRP UNIT**

LIST OF TABLES.....	xi
LIST OF FIGURES.....	xii
LIST OF EQUATIONS.....	xvii
1 Introduction	1
1.1 What is Fiber Reinforced Polymers (FRP)/Composites?	2
1.2 Manufacturing of Composites	3
1.2.1 Advantages of Composites	4
1.2.2 Disadvantages of Composites	5
1.3 Development and Applications of Composites in Civil Engineering	6
2 Literature Review	11
2.1 Previous Research	11
2.2 Hybrid-Composite Unit	13
2.2.1 Small-Scale Units.....	14
2.2.2 Practical Applications.....	18
2.2.3 Australian Approach to Bridges Utilizing FRP Composites.....	20
3 Theoretical Background	24

3.1	Finite Element Analysis	24
3.2	ANSYS Elements	24
3.2.1	Brick Elements	25
3.2.2	Tetrahedral Elements.....	26
3.2.3	Shell Elements.....	27
3.3	Material Model in ANSYS	27
3.3.1	Elasticity	28
3.3.2	Plasticity	28
3.4	3-D Geometry Creation	28
3.5	Finite Element Meshing	29
3.6	Structural Static Analysis in ANSYS	30
3.6.1	Linear Analysis	31
3.6.2	Non-linear Analysis.....	32
3.7	Failure Criteria.....	36
3.8	Initial State	38
3.9	Solution Controls	38
3.9.1	Arc-Length Method	38
3.9.2	Ramped vs Stepped Loading.....	39
3.9.3	Equation Solver Selection.....	40
3.10	Power vs Full Graphics	40

4	Numerical Modeling using ANSYS	42
4.1	Numerical Modeling.....	42
4.2	Element Selection	43
4.2.1	3-D Solid Elements	43
4.2.2	ANSYS Contact Elements.....	43
4.3	Material Models	44
4.3.1	Linear Material Models.....	44
4.3.2	Cohesive Zone Material Model	45
4.4	Creation of the 3-D Model	50
4.5	Meshing	51
4.5.1	Mesh Sensitivity	52
5	Parametric Studies, Discussions, and results	54
5.1	Finite Element Modeling.....	54
5.2	Finite Element Analysis Input	55
5.2.1	Implementation of Geometric Nonlinearities.....	55
5.2.2	Implementation of Contact Elements	56
5.2.3	Failure Sequence (Strain Failure Criteria)	58
5.2.4	Initial Strain	58
5.3	Finite Element Model Verification	59
5.4	Finite Element Model Validation	60

5.5	Adhesive Contact Analysis	66
5.5.1	Concrete-GFRP Adhesive Bond Interface.....	71
5.5.2	GFRP-CFRP Adhesive Bond Interface	76
6	Conclusions and Recommendations	85
	References.....	87

LIST OF TABLES

Table 2.1: Geometric Parameters of the Small-Scale Units (Deskovic & Triantafillou, 1995)	15
Table 2.2: Material Properties of The Small-Scale Units (Deskovic & Triantafillou, 1995)	17
Table 4.1: Concrete, GFRP, and CFRP Material Properties (Deskovic & Triantafillou, 1995)	45
Table 4.2: Bulk Material Properties of Araldite AV138 and Araldite 2015 (Carvalho & Campilho, 2017)	49
Table 4.3: CZM Model Properties (Carvalho & Campilho, 2017)	50
Table 5.1: Non-Linear Solution Controls	56
Table 5.2: Contact Element Key Options Settings	57
Table 5.3: Target Element Settings	57
Table 5.4: Contact Analysis Solution Controls	58
Table 5.5: Ultimate Strain Values (Deskovic & Triantafillou, 1995)	58

LIST OF FIGURES

Figure 1.1: MBrace™ Composite Strengthening System	2
Figure 1.2: Pultrusion Process (Google Images).....	3
Figure 1.3: FRP Wrapping Around Existing Beams (Structure Magazine)	4
Figure 1.4: Eyecatcher Building Basel, Switzerland (Structure Magazine)	7
Figure 1.5: Eyecatcher Load Bearing Elements (Structure Magazine).....	7
Figure 1.6: Knickerbocker Bridge (Google Images)	9
Figure 1.7: Application of FRP Materials for Strengthening Purposes (Structure Magazine)	9
Figure 2.1: Hybrid Composite Unit (Deskovic & Triantafillou, 1995).....	14
Figure 2.2: Locations of The Coupon Specimens (Deskovic & Triantafillou, 1995) .	16
Figure 2.3: Three-Point Load Test Setup for Small-Scale Units (Deskovic & Triantafillou, 1995).....	18
Figure 2.4: Section View of Van Erp's First Composite Bridge (G. Van Erp, 2002) .	20
Figure 2.5: First Composite Bridge in Australia (Jonathaan DePlanche, 2003).....	21
Figure 2.6: Construction of Taromeo Creek Bridge (Queensland Department of Main Roads 2005).....	21
Figure 2.7: Section view of Taromeo Creek Bridge (Google Images).....	22
Figure 2.8: Oregon Road Bridge Section View (O'Connor, 2008)	22
Figure 3.1: Commonly Used Structural Elements in ANSYS.....	25
Figure 3.2: Example of a Brick Element (ANSYS Inc, 2017)	25

Figure 3.3: 10-NodeTetrahedral/SOLID187 (ANSYS Inc, 2017)	26
Figure 3.4: 4-Node Shall Element (ANSYS Inc, 2017)	27
Figure 3.5: Linear Static Force vs Displacement Relation (ANSYS Inc, 2017)	31
Figure 3.6: Non-Linear Force vs Displacement Relation (ANSYS Inc, 2017)	32
Figure 3.7: Newton-Raphson Approximation (ANSYS Inc, 2017).....	33
Figure 3.8: Non-Linear Response (ANSYS Inc, 2017)	34
Figure 3.9: Contact Modeling (ANSYS Inc, 2017)	36
Figure 3.10: 3-D Representative Stress Volume (Timoshenko & Goodier, 1951)....	37
Figure 3.11: Arc-Length Method (ANSYS Inc, 2017)	39
Figure 3.12: Loading Conditions (ANSYS Inc, 2017)	40
Figure 4.1: Finite Element Model Development Flow	42
Figure 4.2: Target and Contact Elements (ANSYS Inc, 2017)	44
Figure 4.3: Failure Mechanisms of Adhesive Bonding	46
Figure 4.4: Triangular CZM Shape Laws (Da Silva & Campilho, 2012).....	46
Figure 4.5: 3-D Hybrid Composite Unit in ANSYS.....	51
Figure 4.6: Boolean Glue Operation (ANSYS Inc, 2017).....	51
Figure 4.7: Hybrid Composite Unit Meshed Model Plot.....	52
Figure 4.8: Mesh Convergence Study Plot.....	53
Figure 5.1: Typical Three-Point Bending Test (Google Images).....	55
Figure 5.2 Load vs Displacement Unit # 14 (dashed line) (Deskovic & Triantafillou, 1995).....	61
Figure 5.3: Load vs Displacement of Unit # 14 FEA Model in ANSYS	62
Figure 5.4: Elevation View of the Deformed Hybrid-Composite Unit	62

Figure 5.5: Top Isometric View of the Hybrid-Composite Unit During FE Modeling	63
Figure 5.6: Bottom Isometric View of the Hybrid Composite Unit During FE Modeling	63
Figure 5.7: CFRP Layer Failure Initiation	64
Figure 5.8: CFRP Layer Complete Failure	65
Figure 5.9: Concrete Layer Complete Failure Elevation View	65
Figure 5.10: Average Strain Distribution Per Loadstep	66
Figure 5.11: Single-Lap Joint During Three Point Bending (Grant, Adams, & da Silva, 2010)	67
Figure 5.12: Joint Under Three-Point Bending (left) and Joint Under Tension (right) (Grant, Adams, & da Silva, 2010)	68
Figure 5.13: Iso View of Half Hybrid-Composite Unit with Constrained Degrees of Freedom During Contact Analyses	69
Figure 5.14: Cross-Section A-A View of Hybrid-Composite Unit with Constrained Degrees of Freedom During Contact Analyses	69
Figure 5.15: Experimental, Analytical, and Numerical $P_m - L_o$ Curves Considering Triangular, Trapezoidal, and Linear-Exponential CZM Laws Araldite AV138 (a) and Araldite 2015 (b) (Carvalho & Campilho, 2017)	70
Figure 5.16: Concrete-GFRP Adhesive Shear Stress Distribution Contour Plot (Araldite 2015)	71
Figure 5.17: Sector A) Concrete-GFRP Adhesive Shear Stress Distribution Contour Plot (Araldite 2015)	72

Figure 5.18: Sector B) Concrete-GFRP Adhesive Shear Stress Distribution Contour Plot (Araldite 2015).....	72
Figure 5.19: Concrete-GFRP Adhesive External Edge Longitudinal Shear Stress Distribution Araldite AV 138 (left) vs Araldite 2015 (right).....	73
Figure 5.20: Concrete-GFRP Adhesive Lateral Shear Stress Distribution at 1/3 of the Span Araldite AV 138 (left) vs Araldite 2015 (right).....	73
Figure 5.21: Concrete - GFRP Adhesive Normal Stress Distribution Contour Plot (Araldite 2015).....	74
Figure 5.22: Sector A) Concrete - GFRP Adhesive Normal Stress Distribution Contour Plot (Araldite 2015).....	75
Figure 5.23: Sector B) Concrete - GFRP Adhesive Normal Stress Distribution Contour Plot (Araldite 2015).....	75
Figure 5.24: Concrete – GFRP Adhesive Layer External Edge Longitudinal Normal Stress Distribution Araldite AV 138 (left) vs Araldite 2015 (right).....	76
Figure 5.25: Concrete – GFRP Adhesive Lateral Normal Stress Distribution at the Center of the Unit Araldite AV 138 (left) vs Araldite 2015 (right).....	76
Figure 5.26: GFRP – CFRP Adhesive Shear Stress Distribution Contour Plot (Araldite 2015).....	77
Figure 5.27: Sector A) GFRP – CFRP Adhesive Shear Stress Distribution Contour Plot (Araldite 2015).....	78
Figure 5.28: Sector B) GFRP – CFRP Adhesive Shear Stress Distribution Contour Plot (Araldite 2015).....	78

Figure 5.29: GFRP – CFRP Adhesive Longitudinal Shear Stress Distribution Plot Araldite AV 138 (left) vs Araldite 2015 (right).....	79
Figure 5.30: GFRP – CFRP Adhesive Lateral Shear Stress Distribution Plot Above the Left Support Araldite AV 138 (left) vs Araldite 2015 (right).....	79
Figure 5.31: GFRP – CFRP Adhesive Normal Stress Distribution Contour Plot (Araldite 2015).....	80
Figure 5.32: Sector A) GFRP – CFRP Adhesive Normal Stress Distribution Contour Plot (Araldite 2015).....	81
Figure 5.33: GFRP – CFRP Adhesive Longitudinal Normal Stress Distribution Plot Araldite AV 138 (left) vs Araldite 2015 (right).....	82
Figure 5.34: GFRP – CFRP Adhesive Lateral Normal Stress Distribution Plot Araldite at the Support AV 138 (left) vs Araldite 2015 (right).....	82
Figure 5.35: Concrete-GFRP Adhesive Bond Damage Initiation.....	83
Figure 5.36: GFRP-CFRP Adhesive Bond Damage Initiation	83
Figure 5.37: GFRP-CFRP Overall Percent of Strain Energy Released Rate.....	84

LIST OF EQUATIONS

Equation 3.1	31
Equation 3.2	32
Equation 3.3	34
Equation 3.4	34
Equation 3.5	35
Equation 3.6	35
Equation 3.7	36
Equation 3.8	37
Equation 4.1	47
Equation 4.2	48
Equation 4.3	48

1 INTRODUCTION

The increasing need for lightweight structures in civil engineering to decrease overall construction costs is growing. Use of adhesive bonding as an alternative to mechanical fasteners in conjunction with composite FRP materials is a way to make structures lighter. However, adhesive bonding between major structural components which are made of FRP materials is not common in civil engineering, even though other industries, such as aerospace, have adopted adhesive bonding of FRP materials long time ago. For example, Boeing 787 and Airbus A350 contains more than 50% of bonded FRP components (He, 2011).

One of the successful designs of bonded FRP materials, is the hybrid-composite unit developed by Deskovic et al. (1995). The unit showed good correlation between theory and results (Deskovic & Triantafillou, 1995). However, during laboratory tests adhesive bond had failed, and mechanical fasteners were added to complete the tests (Deskovic & Triantafillou, 1995). Variations of this unit were used to replace deteriorating bridges in Australia and USA. Because of the success of the hybrid-composite unit, the adhesive bonding between its materials without mechanical fasteners must be studied to further improve its design.

The main objectives of the present study are:

- Contribute to the knowledge of on adhesive bonding between dissimilar materials (concrete to FRP and FRP to FRP)
- Review applications of adhesives and FRP materials in civil engineering

- By means of 3-D non-linear finite element analysis predict failure loads, displacements, and deformations of the hybrid-composite unit (Deskovic & Triantafillou, 1995)
- Evaluate stresses induced in adhesive bondlines of the hybrid-composite unit (Deskovic & Triantafillou, 1995) using two structural adhesives
- Identify bondline locations of stress concentrations
- Compare bond strength of two structural adhesives

The finite element analyses are carried out using ANSYS Mechanical APDL 17.2. The three-point-bending test is the loading mechanism during finite element analyses. The cohesive bond is modeled using finite element analysis with mix-mode cohesive zone model (CZM).

1.1 What is Fiber Reinforced Polymers (FRP) Composites?

Typically, FRP or composite material consists of two distinct independent components: the matrix or base material and a fiber reinforcement. The matrix is a liquid binder that serves as a glue for the fiber reinforcement (see Figure 1.1).

The reinforcement usually is in a fiber form.

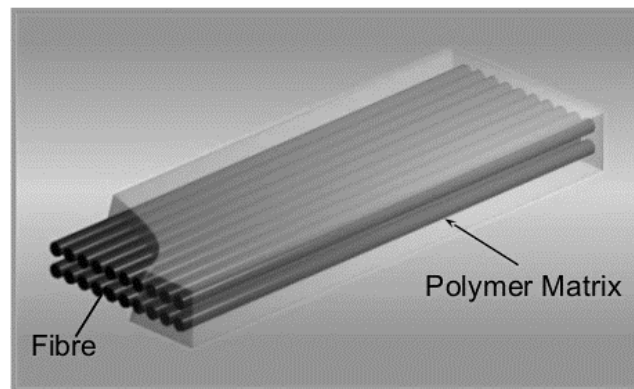


Figure 1.1: MBrace™ Composite Strengthening System

1.2 Manufacturing of Composites

Fabrication of composites is a state-of-the-art process that requires special equipment and high precision. Thus, when it comes to structural engineering projects, it is preferred for all fabrication to be done off site. Prefabricating all the composite components of a structure comes with a better-quality-control, lower installation-labor cost, and reduced construction time. Two manufacturing processes of FRPs are pultrusion and hand layup. Out of the two pultrusion is by far the most popular method to produce structural sections. Figure 1.2 shows a typical composite manufacturing via pultrusion.

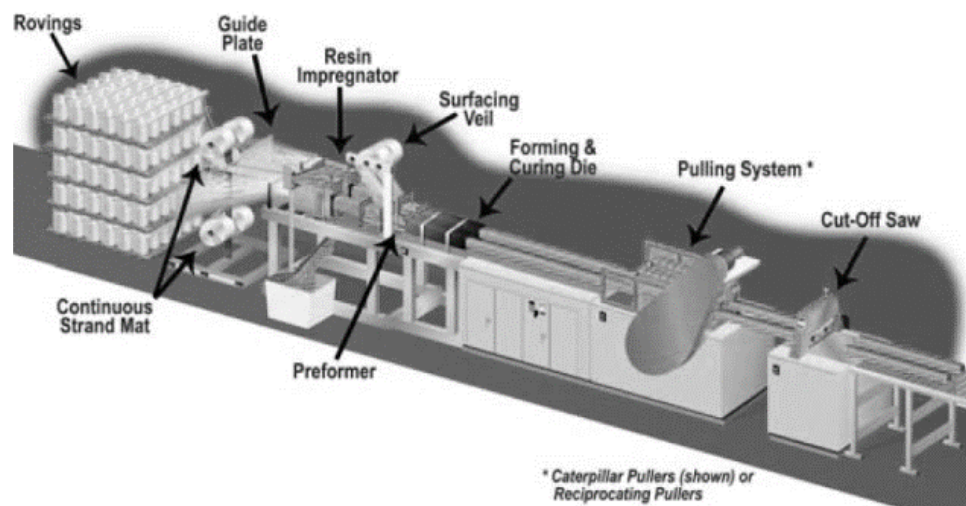


Figure 1.2: Pultrusion Process (Google Images)

The technique involves pulling reinforcement fibers through a resin bath and then through heated die. Pultruded through the matrix, fibers can be molded into any shape. This process is automated and continuous. The benefit of this process is that components of any length can be fabricated (Keller, Theodorou, Vassilopoulos, & de Castro, 2015).

However, layup process provides ability of manufacturing FRP composites on site. Carbon or glass fibers impregnated with resin are wrapped around a desired surface. This flexibility is beneficial in some projects, because the availability of prefabricated shapes is limited; and prefabricated shapes cannot be bent to wrap around columns. For example, projects involving strengthening of existing structures with FRP composites, like the one shown in Figure 1.3, in many cases would utilize layup over pultrusion procedure.



Figure 1.3: FRP Wrapping Around Existing Beams (Structure Magazine)

1.2.1 Advantages of Composites

The advantages of composite materials include: low weight and high strength, greatly improved corrosion resistance and durability. (G. Van Erp, 2002). Composite materials already help engineers in aerospace industry design sustainable and durable structures.

Departments of Transportation in the US need an economical and quick alternative to replace the deteriorating infrastructure (American Society of Civil Engineers, 2017). Use of prefabricated components made of FRP materials will result in high

initial savings, short installation time, and low maintenance cost (O'Connor, 2008). The benefits of the accelerated construction are: decrease of the traffic impacts, improvements to the construction zone safety, and low environmental impacts (O'Connor, 2008).

Furthermore, replacement of heavy existing components with lighter made of composite materials will allow for an increase in loads, without an overall increase of load on the supporting structure (G. Van Erp, 2002). The corrosion resistance of fiber composites can significantly decrease maintenance cost; thus, the whole-of-life cycle cost is often less than for traditional construction materials (Queensland Government Department of Main Roads, 2006).

The high corrosion threshold point is ideal for structures located in high humidity environments. The strength will provide the necessary bearing capacity without loss in safety and security. Light weight will introduce the initial savings in transportation as well as foundation costs. Lastly, the prefabrication of all the components will help to reduce the installation time.

1.2.2 Disadvantages of Composites

Even though composites have been around for a while, they are a new technology in bridge construction. Therefore, like any new technology, composites are facing challenges of “being first”. For example, there is not enough data on long-term performance of composite structures. Structures constructed using composites are relatively young, so the changes in their structural integrity over a long period of time is unknown today.

1.3 Development and Applications of Composites in Civil Engineering

Composite materials are known for their strength, corrosion resistance, and light weight, which makes them perfect material for airplanes. This is precisely the reason why composites were developed originally. With the advancement of the aerospace industry, composites became the material of choice for rockets and other space explorational equipment. Today, composites are widely used in transportation, infrastructure, sport, and medicine.

In recent years, composites have become more popular in the building and construction industries. Today FRP's are used in: bridge repair, bridge design, mooring cables, structural strengthening and stand-alone components. (Halliwell, 2000).

In 1998, the tallest building, named eyecatcher, made of GFRP was built in Basel, Switzerland. The building is five stories high (15 m). All load bearing elements are made of GFRP material and bonded with an adhesive (see Figure 1.5). This building is a pilot structure to break the ground for the future GFRP based structures. Eyecatcher, was assembled twice in its life time. It was assembled for a building fair first and then it was disassembled and reassembled on its destination. This kind of modularity would not be possible with typical construction methods. Figure 1.4 shows eyecatcher building after it was brought to its permanent location. Until this day the building remains in use as an office building.



Figure 1.4: Eyecatcher Building Basel, Switzerland (Structure Magazine)

As was previously mentioned, GFRP elements were made of simple shapes that were bonded with an adhesive (Figure 1.5). Bolted connections were only used when they were absolutely necessary. The elements were made of glass fibers bonded by isophthalic polyester resin. The fibers were composed of chopped strand mats and $0^{\circ}/90^{\circ}$ woven mats, stitched together. The fiber volume fraction was approximately 50%, of which 30% combined mats (Keller, Theodorou, Vassilopoulos, & de Castro, 2015). The outer mats of the elements were polyester surface veil coated.

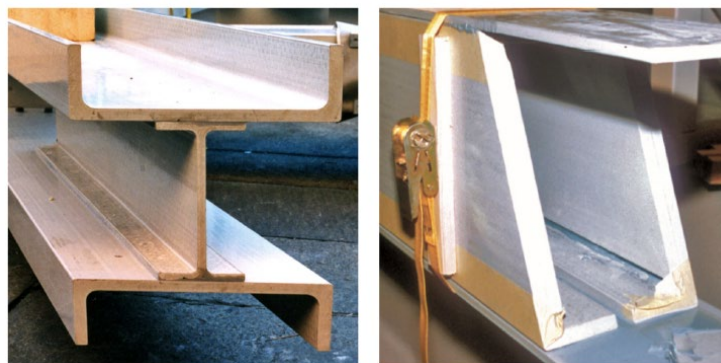


Figure 1.5: Eyecatcher Load Bearing Elements (Structure Magazine)

Structural integrity of Eyecatcher building was investigated twice after 1999. The first investigation in 2006 revealed some fiber blooming on the beams at the top floors as well as some color change between near bolted connections. It was determined that those changes do not affect structural integrity of the building. The second investigation in 2014 did not add anything new to this list. The only change was 5% increase in fiber blooming. Regarding the adhesive bond between the profiles no signs of damage like cracks or debonding were detected (Keller, Theodorou, Vassilopoulos, & de Castro, 2015).

Knickerbocker bridge located in Boothbay Harbor, Maine is the longest bridge in the world that was designed utilizing composite materials (see Figure 1.6). The bridge has eight spans with a total length of 540 feet and is 32 feet wide. The total weights of one girder were 5,250 lbs. and 17,150 lbs. for empty and loaded conditions respectively (Hillman Composite Beam, 2011).

When Maine DOT started reviewing alternatives to solve the deterioration problem of the original 53 years old Knickerbocker bridge, one of the options was to replace it. However, one of the requirements of the new bridge was that it had to be much more resilient than the original to the harsh marine environment. As it was mentioned before, composites are the material of choice for those type of environments. Their main advantages are strength, lightweight, and a corrosion-resistance. In fact, the 70-foot-long girders were so light that one truck was able to transport four of them at once. This would not be possible with standard precast concrete girders (Hillman Composite Beam, 2011).



Figure 1.6: Knickerbocker Bridge (Google Images)

Another accepted application of FRP composites is for strengthening of existing structures (see Figure 1.7). FRP fabrics may be adhered to the tension side of structural members to provide additional tension reinforcement, wrapped around to increase their shear strength, and wrapped around columns to increase their shear and axial strength (Alkbrdaji, 2015). The surface, to which FRP will adhere to, must be cleaned, prepared, and be entirely attached to a structural element. Any concrete deterioration or corrosion of the reinforcement must be fixed prior to bonding of FRP materials. The application of primers and epoxies will improve adhesion of FRPs. Most resins are sensitive to UV light, thus protective coating is also necessary to preserve integrity of FRP system.



Figure 1.7: Application of FRP Materials for Strengthening Purposes (Structure Magazine)

Thesis is organized in the following format:

Chapter 1 – Introduction

Chapter 2 – Literature Review

Chapter 3 – Theoretical Background

Chapter 4 – Numerical Modeling Using ANSYS

Chapter 5 – Parametric Studies, Discussions, and Results

Chapter 6 – Conclusions and Recommendations

2 LITERATURE REVIEW

For decades civil engineering industry has been searching for solutions to make structures lighter to decrease construction costs. Use of adhesive bonding as an alternative to mechanical fasteners is a way this can be achieved. Additionally, the increase of lightweight materials available on the market, such as FRP, promotes use of adhesive bonding (He, 2011). Aerospace industry was the first to experiment with adhesive joints successfully. Today, most of automobile and aerospace components are joined by adhesives (Kadam, Firake , & Pawar, 2015). Thus, through this and similar studies adhesive joints will become a common practice in civil engineering.

Research on stress concentrations and strength analysis of adhesive joints is ongoing (Kadam, Firake , & Pawar, 2015). It is constantly being updated by the industries and academia. Simultaneously, FE software packages are expanding their tools to model adhesive joints. In many fields use of sophisticated computational tools, based on FE analysis, provides means for analysis and design. FE analysis is a widely used to analyze adhesive joints. It allows for simulations and optimizations of different adhesive joint designs prior to testing and manufacturing.

2.1 Previous Research

M. S. Kadam (2015) studied effects of varying load and thickness of the adhesive layer on stress induced in the adhesive single lap joint of two Aluminum plates

under tensile loading. Results from FEA software RADIOSS were compared with the experimental work. It was reported that strength of the joint decreases with increase in thickness of the adhesive. Stress in the joint was found to be directly proportional to the applied load. Additionally, a strong agreement was observed between FE and experimental results.

Mohammed Waseen H. S. (2014) analyzed delamination of a Double Cantilever Beam specimen by means of two different computer aided methods: Virtual Crack closure Technique (VCCT) and Cohesive Zone Method (CZM). The load vs displacement curve predicted via Cohesive Zone Method agreed well with the results. It was observed that VCCT overestimates the critical load. The results were validated by the work published in Benchmarks for Composite Delamination Publication R00084: NAFEMS, 2002 authored by G.A.O. Davies. Additionally, the parametric study showed that changing height of the specimen results in a higher failure load.

Jakub Korta (2014) compared FE results of adhesive bonds using CZM with experimental results. The study used two different FE element types (brick and shell) to model adhesive layer, both types were modeled with CZM. It was concluded that CZM method can be used to model adhesive joints, while preserving the required accuracy. Both types of FE elements have yielded accurate results.

Kumar et al. (2010) investigated behavior of the single-lap joint bonded by two different adhesives simultaneously (bi-adhesive bond). The two adhesives were ESP110 and DP490, which are different in their stiffnesses. ESP110 epoxy is

stiffer than DP490 epoxy. Both adhesives are off the shelf generally sold products. The study concluded that stress concentrations at the edges of the single-lap joint can be reduced through employing graded stiffness bonding. Ductile epoxy is placed at the edges while rigid epoxy is situated in the center of joint. Their analysis revealed existence of complex 3-D state of stress/strain through interior of the single-lap joint. Through experiments, they concluded that because of the complex 3-D state of stress/strain the plane strain analysis overestimates structural strength of the joint.

Campilho et al. (2013) have analyzed effects of CZM law shapes (triangular, exponential, or trapezoidal) on strength predictions of the adhesive layer in a the single-lap joint. The single-lap joints were bonded with ductile and brittle adhesives with varying overlap distance. The study showed that trapezoidal shape best suited for joints bonded with a ductile adhesive. However, triangular shape can be used since it underpredicts the joint strength. Additionally, the study concluded that the influence of CZM shape is greater for smaller overlap distances.

2.2 Hybrid-Composite Unit

Deskovic and Trintafillou's research published in the ASCE Structural Engineering journal in 1995 introduced a hybrid-composite unit with design procedures that were supported by experimental and analytical work (see Figure 2.1). Their research demonstrated strong correlation between theory and experiments. The proposed hybrid-composite unit joined CFRP, GFRP, and concrete materials through adhesive and mechanical bonding utilizing their strongest mechanical

characteristics. Deskovic et al. claimed that their design results in a low cost, low weight, and high-performance unit with pseudo-ductile characteristics.

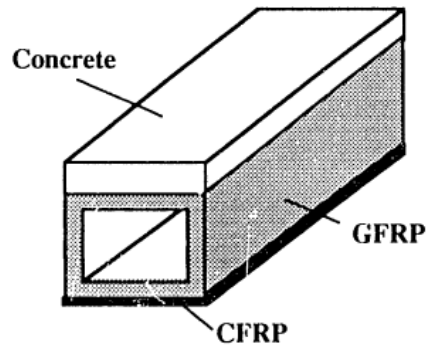


Figure 2.1: Hybrid Composite Unit (Deskovic & Triantafillou, 1995)

In their study, Deskovic et al. (1995) have analyzed short and long-term behavior of their hybrid-unit. However, only the short-term behavior analysis of their hybrid composite unit is referenced in this study. The short-term behavior was studied through experimental work and numerical analysis. For the experimental work, Deskovic et al. (1995) have had manufactured 18 small scale and 7 large scale units (only units 1,3, and 4 were used to for short-term analysis). The numerical analysis was carried out using finite element software MARC/MENTAT 1990. Experimental and numerical results showed good agreement with theory (Deskovic & Triantafillou, 1995).

2.2.1 Small-Scale Units

The small-scale units had standard pultruded GFRP box, 60x80 mm, with the web thickness of 3 mm and flange thickness of 4 mm, and varying span 0.45 – 1.4 m. The small-scale units had different dimensions for the concrete and CFRP layers

as well. Additionally, two concrete mix designs and two different types of CFRP laminates were utilized to manufactured small-scale units.

To bond all three material two-component epoxy based structural adhesive Araldite was used (density 0.0014 g/mm³ and thickness about 0.5 mm). This adhesive is usually used for the construction joints. In their study Deskovic and Triantafillou used high failure strain CFRP, that had to be pretensioned prior to bonding with GFRP. Different failure modes were encountered by changing the span length, thus switching from shear to flexure governed modes. Table 2.1 summarizes geometric design parameters of the small-scale beam used in experimental short-term analysis.

Table 2.1: Geometric Parameters of the Small-Scale Units (Deskovic & Triantafillou, 1995)

Beam	Concrete Type	Concrete Thickness [mm]	CFRP Type	CFRP Thickness [mm]	Pretension Strain [%]	Span Length [m]
1	-	-	-	-	-	0.50
2	normal	25	-	-	-	0.90
3	normal	25	G/CFRP	0.30	-	1.40
4	normal	25	G/CFRP	0.30	0.58	1.40
5	normal	15	G/CFRP	0.30	-	0.65
6	normal	25	G/CFRP	0.30	-	0.50
7	normal	31	G/CFRP	0.30	-	1.40
8	normal	31	G/CFRP	0.26	0.63	1.40
9	normal	15	G/CFRP	0.30	-	0.50
10	normal	31	CFRP	0.45	-	0.40
11	normal	25	-	-	-	1.40
12	normal	25	G/CFRP	0.30	-	0.90
13	HS-FRC	28	G/CFRP	0.30	-	1.40
14	HS-FRC	28	G/CFRP	0.30	0.34	1.40
15	HS-FRC	28	G/CFRP	0.30	-	0.65
16	HS-FRC	15	G/CFRP	0.30	-	0.50
17	HS-FRC	28	-	-	-	1.05
18	-	-	-	-	-	1.40

The pultruded GFRP box was comprised of various layers bonded with a polyester matrix. The exact composition of those layers was determined by burn-off technique. Starting from outside the layers were: 1) mat of randomly oriented

bounded fibers, 2) two-directional 0/90 fibers, 3) unidirectional roving, 4) mat of randomly oriented bounded fibers, 5) two-directional 0/90 fibers, 6) mat of randomly oriented bounded fibers. The volume fraction of the glass fibers was about 30%. The walls had approximately the same fiber content per wall surface (Deskovic & Triantafillou, 1995).

Total of 16 coupon specimens were cut of the GFRP profile according to German DIN (No. 3 of DIN 53 455). The coupons were subjected to uniaxial tension test to develop corresponding stress-strain curves. Figure 2.2 displays the locations of the coupon's specimens.

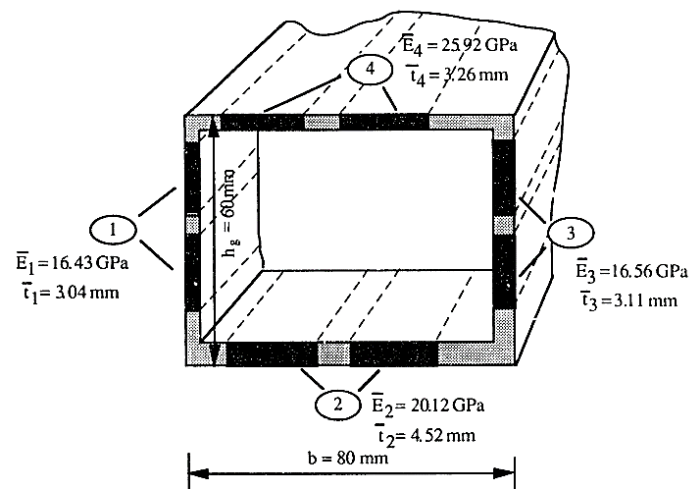


Figure 2.2: Locations of The Coupon Specimens (Deskovic & Triantafillou, 1995)

Two concrete types were used in small-scale units. 1) normal strength 2) high strength carbon fiber reinforced HS-FRC containing silica fume. For the CFRP layer two different CFRP were used: 1) carbon/epoxy, 2) carbon/glass/epoxy (G/CFRP). The CFRP sheets were unidirectional. CFRP sheet must be very thin with strain at failure lower than concrete strain to insure CFRP sheet failure precedes concrete crushing. However, CFRP sheets available to Deskovic at the

time of his research had very high strain at failure. Therefore, his solution was to pretension CFRP prior to bonding it to the GFRP. Table 2.2 summarizes material properties of the small-scale beams.

Table 2.2: Material Properties of The Small-Scale Units (Deskovic & Triantafillou, 1995)

Property	Notation	Units	Value
Elastic modulus of concrete	E_c	MPa	Normal: 33400 HS-FRC: 19400
Compressive strength of concrete	f'_c	MPa	Normal Strength: 40 HS-FRC: 58
Tensile strength of concrete ¹	f'_t	MPa	Normal: 4.45
Ultimate concrete strain	ϵ_c^u	%	Normal: 0.38 HS-FRC: 0.50
Elastic modulus of CFRP	E_2	MPa	G/CFRP: 80235 CFRP: 110000
Ultimate CFRP strain	ϵ_2^*	%	G/CFRP: 1.15 CFRP: 1.05
Longitudinal elastic modulus of GFRP	E_3 E_1 E_w	MPa	Top: 25920 Bottom: 20120 Web: 16490
Transverse elastic modulus of GFRP top flange	E_{1T}	MPa	8000
Shear modulus of GFRP web ²	G_w	MPa	2000
Longitudinal Poisson's ratio for top GFRP flange ³	ν_L	-	0.33
Transverse Poisson's ratio for top GFRP flange ³	ν_T	-	0.10

The three-point bending tests were carried out, on small-scale units, using INSTRON 1521 machine with load capacity of 200 kN (see Figure 2.3). The mid-span deflection was measured using a linear voltage differential transducer (LVDT). The age of the beams was between 30 – 45 days. The deflection of the supporting frame was measured separately to correct the LVDT deflection.

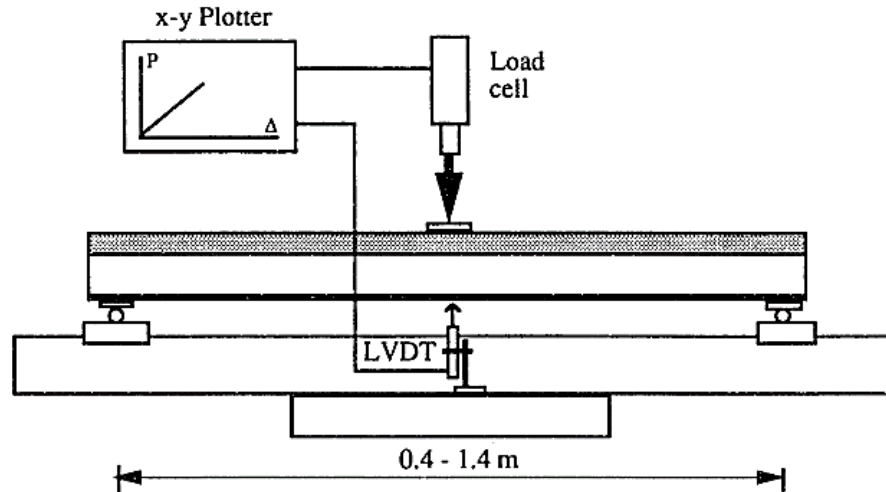


Figure 2.3: Three-Point Load Test Setup for Small-Scale Units (Deskovic & Triantafillou, 1995)

The load vs deflection curves produced by their experimental work on small-scale units can be found in the appendix of this study. However, to summarize the results the average ratio of analytical to experimental ultimate load values was 95.9% while the standard deviation was only 0.066. The average ratio of analytical to experimental stiffness value was 96.5% with standard deviation of 0.052 (Deskovic & Triantafillou, 1995).

2.2.2 Practical Applications

Later Deskovic and Triantafillou's (1995) research was applied to develop a hybrid-composite unit involving the Australian: academia, construction company (Wagner Composite Fiber Technologies (Wagner CFT)), and government. In 2002, Australian academic Van Erp developed a composite unit that had a slight modification of the unit developed by Deskovic and Triantafillou. In his paper "An Australian Approach to Fiber Composite Bridges", Erp cites Deskovic's research and states the changes he made to improve Deskovic's composite unit. He

explained that the pultruded GFRP box does not work in Deskovic et al. design because the thickness of the top GFRP flange is negligible. Thus, by accounting for the thickness of the top flange he was able to manufacture Deskovic and Trintafillou's unit using pultruded GFRP box. The contribution is a decrease in manufacturing and handling costs while increase in overall precision during manufacturing. Therefore, having an ability to use a pultruded GFRP box will certainly result in a higher quality product at a lower cost.

Further, the results from load-tests on Erp's modified composite unit were satisfactory. As an experiment, a short span bridge was constructed the same year in Toowoomba, Australia with the help of Wagner CFT. Figure 2.4 shows the prefabricated composite panel developed by Van Erp and used for the full-scale bridge in Toowoomba in 2002. Unfortunately, no public record was found outlining details of Erp's design methodology.

Since the experiment in Toowoomba in 2002, several bridges were constructed in Australia by Wagner CFT, using the hybrid-composite unit comprising of concrete, GFRP, and CFRP in the last seventeen years. Additionally, one bridge was installed in Erie County, United States. In 2004, Wagner CFT manufactured the bridge in Australia and then shipped it to the United States. The following section details the evolution, with examples, of the Deskovic, Trintafillou, and Erp's composite unit in Australia and US.

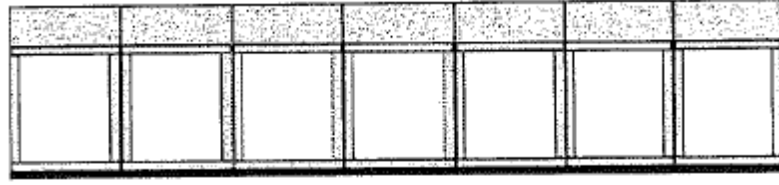


Figure 2.4: Section View of Van Erp's First Composite Bridge (G. Van Erp, 2002)

2.2.3 Australian Approach to Bridges Utilizing FRP Composites

United States is not the only country that experiences infrastructure issues. Australia, for example, has similar situation with their bridges. Queensland – one of the Australian states – has 317 timber bridges in their bridge-inventory. Queensland Department of Transportation has plans to replace all the timber bridges with bridges made of more durable and sustainable material like FRP.

Queensland's government collaborated with academia and local industries to develop engineering concepts to replace timber bridges. Their collaboration produced the first 90-meter span bridge made of concrete, GFRP, and CFRP materials bonded together in Australia. It was built of units developed by Van Erp', which again was a modification of Deskovic et al. research. This bridge was prefabricated and installed in 2003 in northern New South Wales, Australia over Orara River. Figure 2.5 shows the installation of the first hybrid-composite bridge in Australia.



Figure 2.5: First Composite Bridge in Australia (Jonathaan DePlanche, 2003)

Another bridge manufactured by Wagner CFT using similar design was the Taromeo Creek bridge, installed in 2005 on the D'Aguilar Highway at Blackbutt in Queensland, Australia, see Figure 2.6. The traffic volume over this bridge is about 2,500 vehicles per day with 16% of them being heavy vehicles according to 2005 traffic data. The section view of Taromeo Creek Bridge is shown in Figure 2.7. The bridge is 9-meter-wide and 12-meter-long.



Figure 2.6: Construction of Taromeo Creek Bridge (Queensland Department of Main Roads 2005)

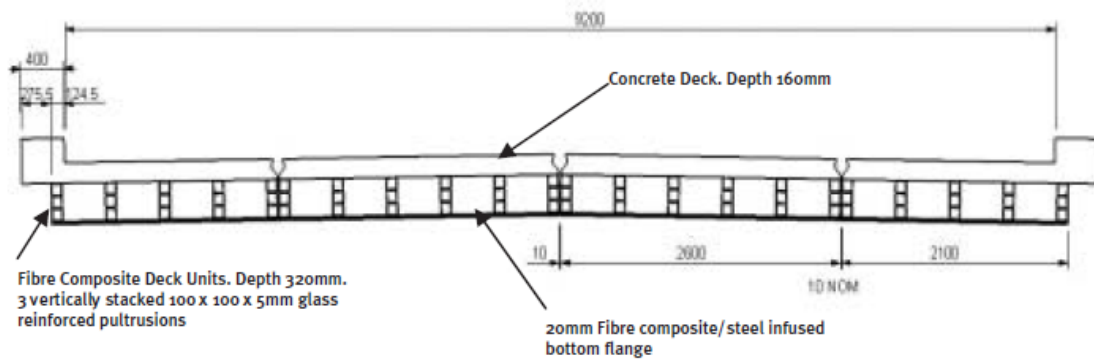


Figure 2.7: Section view of Taromeo Creek Bridge (Google Images)

The bridge in Erie County NY, United States on Oregon Road is an example of a speedy and efficient replacement of a short span bridge. The bridge was constructed using accelerated bridge construction and included benefits such as lightweight, low maintenance, and the service life of 100 years. Figure 2.8 shows the section view of one of the four prefabricated composite superstructure panels. The panels were installed in two days. The total length of the project was 31 calendar days. The county's contractor used a small crew and light equipment to demolish the old bridge, install a modular substructure, and have a completely new bridge ready for traffic in 1/3 the time of a conventionally handled project (O'Connor, 2008).

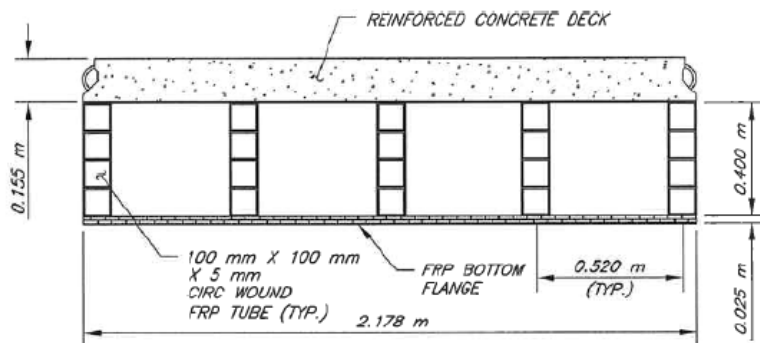


Figure 2.8: Oregon Road Bridge Section View (O'Connor, 2008)

All the bridge replacement projects mentioned above were erected utilizing composite units made of FRP materials and concrete bonded together and designed by Wagner FCT. According to Australian Reinforced Plastics Research and Development journal, Wagner FCT's prefabricated panels are similar to those developed by Van Erp in 2002, whose work improves the composite unit developed by Deskovic et al. in 1995.

3 THEORETICAL BACKGROUND

3.1 Finite Element Analysis

The finite element (FE) method is a mathematical technique for setting up and solving systems of partial differential equations. (Thompson & Thompson, 2017). The present study uses finite element modeling software ANSYS 17.2 to analyze a response of an adhesive bond of a hybrid composite unit, consisting of a combine action of FRP and concrete materials, due to an applied load. Contrary to the closed-form analyses, FE methods permits analysis of any type of geometry. Thus, it considers adherend's shape and the adhesive fillet (Da Silva & Campilho, 2012).

3.2 ANSYS Elements

ANSYS contains comprehensive library of elements. Each element comes with its own characteristics, input, and output data with some of the elements being more common than others because of their historically-reliable outputs. Figure 3.1 illustrates the three category of elements that are historically known as reliable and commonly used for static structural modeling.

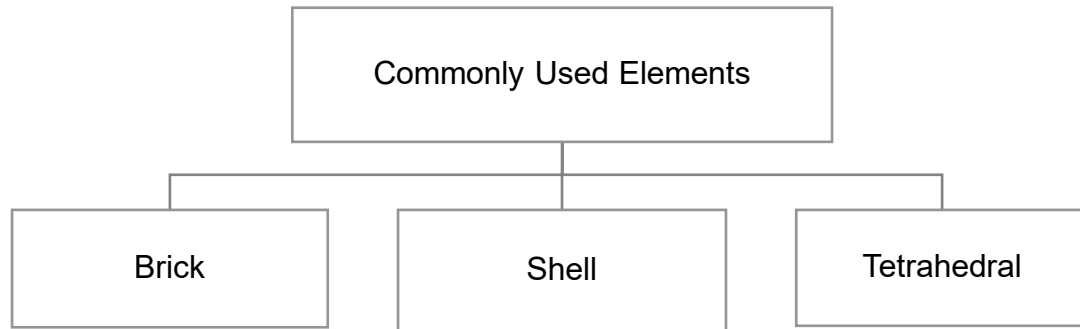


Figure 3.1: Commonly Used Structural Elements in ANSYS

3.2.1 Brick Elements

Brick elements are members of the 3-D solid group in ANSYS. They can have 8, 10, or 20 nodes per element and are known to produce precise results in structural, thermal, and dynamic simulations. Regardless of the node count, each node always has three degrees of freedom (DOF) translations in x, y, z directions. Figure 3.2 demonstrates an example of a brick element.

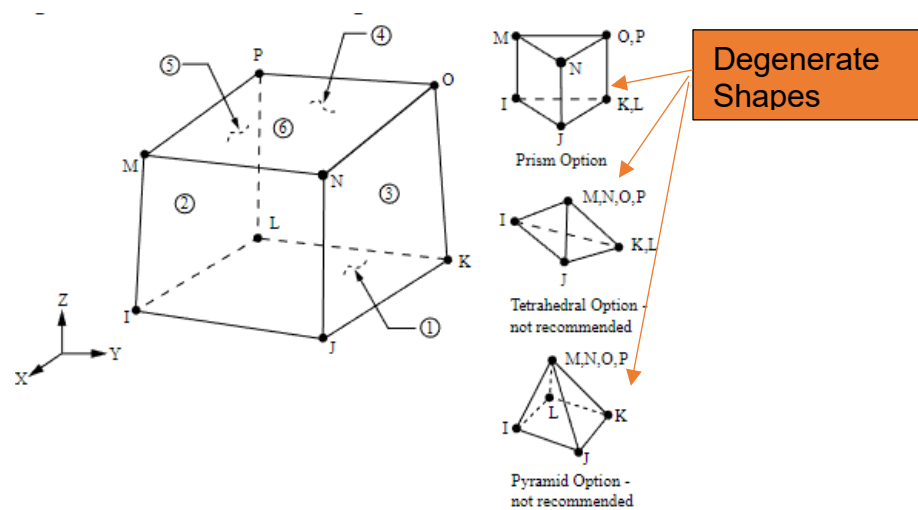


Figure 3.2: Example of a Brick Element (ANSYS Inc, 2017)

Brick elements are known to be forced by ANSYS into degenerate shapes during meshing geometries that could not be meshed otherwise. Once formed into degenerate elements (see right side of Figure 3.2), elements lose nodes, which means they lose terms in their shape functions. Thus, they become stiffer. For example, compressing an eight-node brick element into a four-node tetrahedron reduces the number of independent nodes by half (Thompson & Thompson, 2017).

3.2.2 Tetrahedral Elements

Tetrahedral elements are also members of the 3-D solid group of elements with three translational degrees of freedom at each node. Figure 3.3 shows the shape of Tetrahedral element. Nodes P , R , Q , O , M , N are mid-side nodes. To determine displacements at each node of the element, ANSYS uses quadratic shape functions. Elements with mid-side nodes are known to produce more accurate results over elements without mid-side nodes. As a standard of practice those elements are called higher order elements.

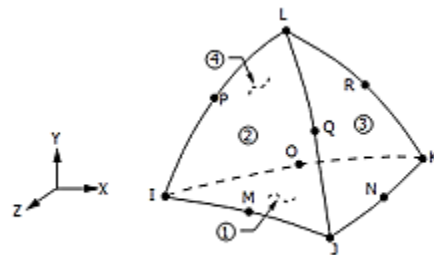


Figure 3.3: 10-Node Tetrahedral/SOLID187 (ANSYS Inc, 2017)

In comparison to Brick elements, Tetrahedral elements are less likely to become degenerate. Therefore, they are often used to mesh geometries that could not be meshed with brick elements without sacrificing accuracy of the results. All the

aforementioned features of Tetrahedral elements distinguish them from the rest the solid elements and make them preferable for non-linear analysis when dealing with geometries that force other elements become degenerate.

3.2.3 Shell Elements

Shell elements are commonly used to model thin structural components. Shell elements decouple deformation on the surface and in the normal direction. This allows for a simple and efficient simulation of a thin structures (ANSYS Inc, 2017). Therefore, they are popular among researchers of composite materials. Figure 3.4 shows 4-node shall element.

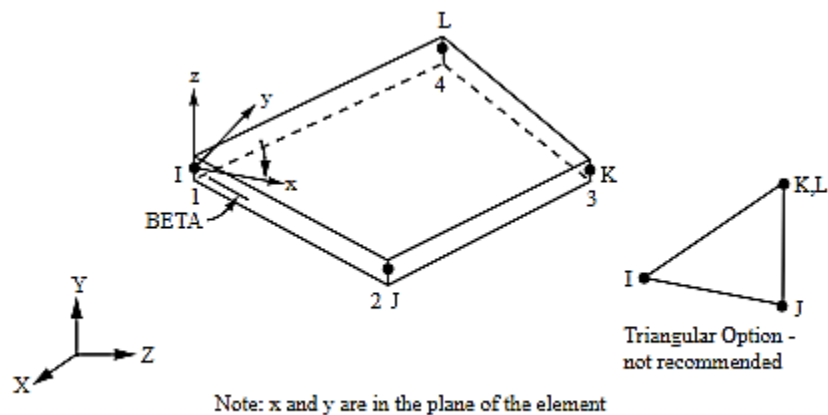


Figure 3.4: 4-Node Shell Element (ANSYS Inc, 2017)

The disadvantage of shell elements is their inapplicability towards irregular geometries. Currently, ANSYS is unable to mesh, using shell elements, hollow rectangular tubes.

3.3 Material Model in ANSYS

A material model is a mathematical representation of the expected behavior of a material (Thompson & Thompson, 2017). For example, it provides a relationship

between stress and strain, heat flux and temperature gradient etc. Material models also assist in simulating behavior such as friction and debonding.

Material Model properties depend on the type of an analysis in the FE software. The two types of analysis used widely are linear and non-linear. A more detailed discussion on those is presented further in this section. Linear analysis material model excludes plasticity and the material is assumed to behave elastically. Plasticity comes into play, when it is of interest to include material nonlinearities into the analysis in ANSYS.

3.3.1 Elasticity

Elasticity is the behavior of a material prior to yielding. It is widely acceptable to assume that strain will completely recover if stress in a material is less than the yield stress. Thus, small strain theory is valid.

3.3.2 Plasticity

Plasticity deals with a material's performance beyond the yield point. Plasticity is also important as an energy-absorbing mechanism for structures in service (ANSYS Inc, 2017).

3.4 3-D Geometry Creation

Top down is one of the two ways to create a 3-D model in ANSYS. The top down modeling encompasses generation of 3-D primitive shapes (rectangle, blocks, etc.) defined by parameters like: height, depth, width etc. Next, the lower order objects (lines, keypoints, etc.) are generated automatically. In general, geometries must be modeled with precision. Symmetry shall be utilized to reduce the size of the model, thus reducing the number of calculations (Da Silva & Campilho, 2012).

All geometries in this study were created using top-down solid modeling procedures.

3.5 Finite Element Meshing

Meshing divides a geometry into finite elements with nodes to model and analyze its behavior under loading. Mesh is at the heart of the finite element modeling procedure. The quality of a finite element model is dependent on the quality of its mesh (Thompson & Thompson, 2017). Even though it is not a complicated procedure, if geometry is not meshed correctly the results will be affected, which may lead to wrong engineering decisions.

There are two aspects of meshing that will affect the results: quantity and shape of elements. There is no rule of thumb to determine the perfect quantity of a mesh. Every problem must be assessed independently. However, an acceptable way to arrive at a satisfactory meshing is to continuously increase element density until results start to converge to a single solution.

Finer mesh is necessary to capture stress concentrations and stress gradients. However, in some cases mesh refinement may not yield convergence due to stress singularities. Application of elasto-plastic or fracture mechanics analyses will suite this situation better (Da Silva & Campilho, 2012).

The shape of every element in ANSYS is checked via shape testing automatically. Shape testing checks the following: element aspect ratio, the deviation from the element's optimal angles, deviation from a parallel state, maximum angle in the element, Jacobian ratio, and element warping factor (Thompson & Thompson, 2017). If any of the characteristics exceed its threshold value, ANSYS will generate

either error or warning. Warning messages do not present threat to accuracy of the results. However, a warning message that says elements were forced into degenerate shapes should be taken seriously. As was mentioned previously elements that have degenerate shapes will produce unreliable results.

3.6 Structural Static Analysis in ANSYS

Static analysis is used to determine parameters: reactions, stresses, strains etc. under static loading. Static analysis can be linear or non-linear. Non-linear static analysis determines the same parameters, while considering one or more of the following: large deflections, material plasticity, stress stiffening, large strains, hyperelasticity, contact behavior, and creep.

The primary degrees of freedom (DOF) calculated in ANSYS structural analysis are nodal displacements, also called primary data. The stresses, strains, reactions, etc. are then calculated from the nodal displacements, also called derived data. The displacements of a node at an intersection of multiple elements are referenced among those elements for further element displacement calculation. At an element level, all referenced displacements from the nodes attached to that element are then averaged to calculate displacement of that element. Similar procedure is used to calculate derived data over an entire model. The element solution data represents the behavior of the model. It is mainly used for model verification (Thompson & Thompson, 2017)

The averaged nodal solution data is calculated by extrapolating the element solution data back to the nodes. Then element solution data is averaged from all elements attached to a node. This process is the same for each node. Nodal

results provide a better estimate of the true values of the stresses, strains, etc. (Thompson & Thompson, 2017). Nodal results are used for model validation.

3.6.1 Linear Analysis

ANSYS linear static structural analysis generally assumes stiffnesses and applied loads remain constant during the analysis. These assumptions are typical for linear analysis in a FEM software. The settings to maintain conditions at which these typical assumptions hold true are: linear elastic material behavior, small deflection theory, no time varying forces, and no internal effects (mass and/or damping). Figure 3.5 is a graphical representation of the linear analysis in a FE software.

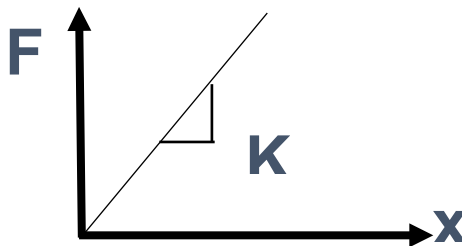


Figure 3.5: Linear Static Force vs Displacement Relation (ANSYS Inc, 2017)

The unknown forces and displacements are found from the matrix (3.1); stresses and strains are then determined based on displacements.

$$[K]\{X\} = \{F\} \quad (3.1)$$

$[K]$ – global stiffness matrix; $\{X\}$ – global displacement vector; $\{F\}$ – global force vector. The material properties required for a linear analysis are Young's Modulus and Poisson's Ratio. Density in ANSYS is specified, if effects of self-weight are to

be considered. Since applied forces are assumed to be constant, the analysis is carried out in one load step.

3.6.2 Non-linear Analysis

In non-linear static analysis stiffness is not constant. It is a function of displacement or material modulus or both. (4.3 represents the global solution matrix equation for non-linear analysis.

$$[K(x)]\{X\} = \{F\} \quad (3.2)$$

Figure 3.6 demonstrates the non-linear relation between force and displacement. The change of variable “x” is what forces the non-linear response. In contrast, to linear analysis the doubling of applied the force does not result in the doubling of the displacement.

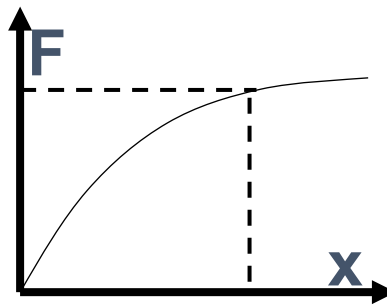


Figure 3.6: Non-Linear Force vs Displacement Relation (ANSYS Inc, 2017)

Non-linear analysis is an iterative procedure since correlation between force and displacement is not linear. The load is applied gradually in multiple load increments (load steps). According to the solution hierarchy in ANASYS, steps can be divided into multiple substeps. At every substep program performs up to 25 iterations to

determine the difference between the applied loads and the loads corresponding to the elements' stresses. If the difference is within the specified convergence criteria, then that substep has converged. During this process the stiffness matrix is adjusted at every iteration. This method is known as Newton-Raphson Method (see Figure 3.7). Out of many nonlinear analysis types only three most common are considered in this study: geometric, material, and contact.

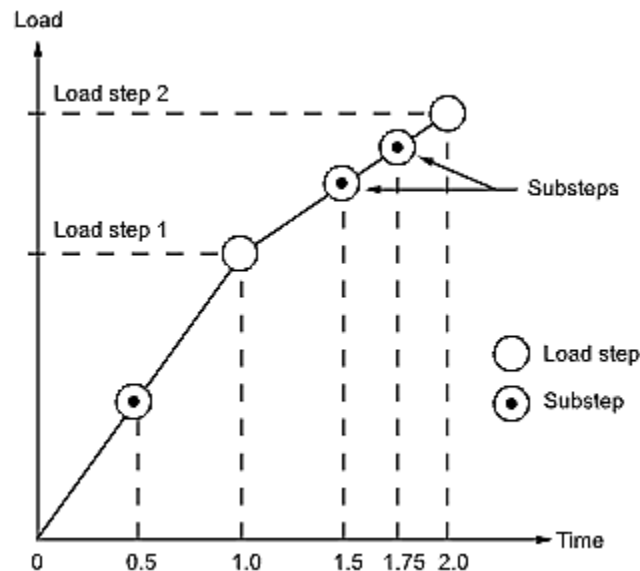


Figure 3.7: Newton-Raphson Approximation (ANSYS Inc, 2017)

3.6.2.1 Geometric Nonlinearity

Under large deformations/displacements and /or rotations, when plane section does not remain plane, a structure's response to loading can be non-linear. An example of non-linear response shown in ANSYS is a fishing rod shown in Figure 3.8. To reflect this in ANSYS the stiffness matrix is adjusted at every load iteration to reflect the change in geometry of the member's section.

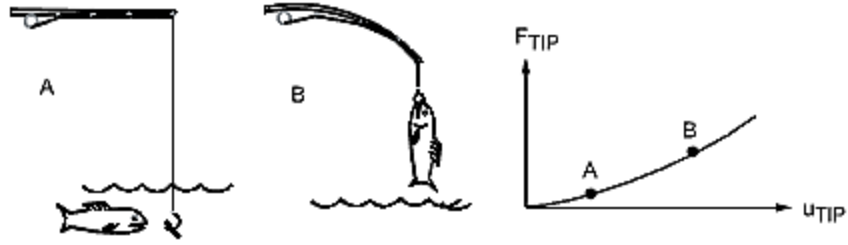


Figure 3.8: Non-Linear Response (ANSYS Inc, 2017)

3.6.2.2 Material Nonlinearity

Materials are known to behave non-linearly beyond the yielding stress. In the plastic region of the stress-strain curve the modulus of elasticity does not remain constant, and the stiffness matrix is modified at every load step. The factors that can influence stress-strain relation include: temperature, load history, and creep.

In the material nonlinearity modeling, stresses and strains are expressed in terms of *true* stresses and strains. To account for the non-linear relationship between stress and strain during modeling, true stress-strain curve is given as input to ANSYS. For large deformations the true stresses and strains are obtained using the following formulations:

$$\epsilon_{\text{true}} = \ln(1 + \epsilon_{\text{eng}}) \quad (3.3)$$

$$\sigma_{\text{true}} = \ln(1 + \sigma_{\text{eng}}) \quad (3.4)$$

3.6.2.3 Contact Nonlinearity

There are different cases of contact analyses in ANSYS. Essentially, contact analysis comprises of a non-linear analysis within a non-linear analysis. Since to model contact between components ANSYS uses Newton-Raphson non-linear

algorithm on top of modeling non-linear behavior of the components themselves. Due to this, contact analysis is highly nonlinear procedure, that requires significant CPU resources (ANSYS Inc, 2017).

In general, contact happens when two bodies touch each other. The common expectation is that surfaces that are in contact do not interpenetrate. However, they can transmit compression, tangential friction, and tension in the case of fully bonded contact. Unfortunately, it is impossible to simulate contact numerically without some penetration. It is analyst's responsibility to assure that the penetration does not have a significant effect on the results (ANSYS Inc, 2017).

For the contact analysis of solid bodies ANSYS uses two penalty-based formulations. (3.5 and (3.6 are examples of the Pure Penalty and Augmented Lagrange formulations respectively (ANSYS Inc, 2017).

$$[K_{normal}] \{X_{penetration}\} = \{F_{normal}\} \quad (3.5)$$

$$[K_{normal}] \{X_{penetration}\} = \{F_{normal} + ALPHA\} \quad (3.6)$$

Where: K_{normal} is a contact stiffness; $X_{penetration}$ is the penetration between surfaces matrix; F_{normal} is the contact force matrix. A high contact compatibility (decrease in penetration) increases quality of the solution. To enforce contact compatibility ANSYS has contact stiffness multiplier FKN . Increasing FKN factor will increase contact stiffness and decrease penetration. FKN range is from 0.1 to 100. The suggested values of FKN for fully bonded contact in ANSYS documentation is ten. To model contact ANSYS meshes areas in contact with contact and target elements. Usually an area made of a more rigid material is assigned target

elements. However, this is not critical for members having similar rigidity. Figure 3.9 shows a graphical representation of a contact model in ANSYS.

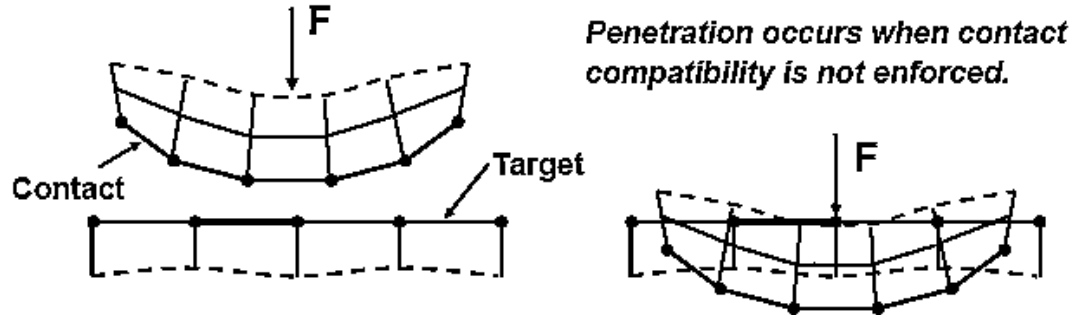


Figure 3.9: Contact Modeling (ANSYS Inc, 2017)

Similar to a non-linear analysis, stiffness matrix in a contact analysis changes with every iteration based on materials, penetration, element thickness etc.

3.7 Failure Criteria

Failure criteria are used to determine the probability, location, and time of failure of a material. It predicts only first occurrence of failure and it is unable to track failure propagation until complete failure (Barbero, 2014). Failure criteria become useful when orthotropic materials are included in a model (Da Silva & Campilho, 2012). In this study maximum-strain-failure criterion is used to assess the failure of the materials used in hybrid composite unit. This criterion is expressed using notation of failure index defined by (3.7), which is the way ANSYS defines failure criterion.

$$I_F = \frac{\text{strain}}{\text{max. strain}} \quad (3.7)$$

This criterion was chosen because strain is assumed to vary linearly within a composite-material-section in contrast to stress. Therefore, it is a more reliable

failure criterion. (4.3 illustrates maximum strain failure criteria formulations in ANSYS.

$$I_F = \max \left\{ \begin{array}{l} \frac{\varepsilon_z}{\varepsilon_t} \text{ if } \varepsilon_z > 0 \text{ or } \frac{-\varepsilon_z}{\varepsilon_c} \text{ if } \varepsilon_z < 0 \\ \frac{\varepsilon_x}{\varepsilon_t} \text{ if } \varepsilon_x > 0 \text{ or } \frac{-\varepsilon_x}{\varepsilon_c} \text{ if } \varepsilon_x < 0 \\ \frac{\varepsilon_y}{\varepsilon_t} \text{ if } \varepsilon_y > 0 \text{ or } \frac{-\varepsilon_y}{\varepsilon_c} \text{ if } \varepsilon_y < 0 \\ \text{abs}(\gamma_{xz})/\gamma_{xzu} \\ \text{abs}(\gamma_{yx})/\gamma_{yxu} \\ \text{abs}(\gamma_{zy})/\gamma_{zyu} \end{array} \right\} \quad (3.8)$$

The quantities in the denominator are the ultimate strains of the material in a given direction. The subscripts denote: (t) tension, (c) compression, (z) longitudinal axis, (x) transverse axis, and (y) vertical axis; see Figure 3.10 for the orientation of all three axes and location of all stresses on a finite representative 3-D volume. Possible failure of a material is evaluated at the top and bottom (or middle) of each layer at each of the in-plane integration points (ANSYS Inc, 2017).

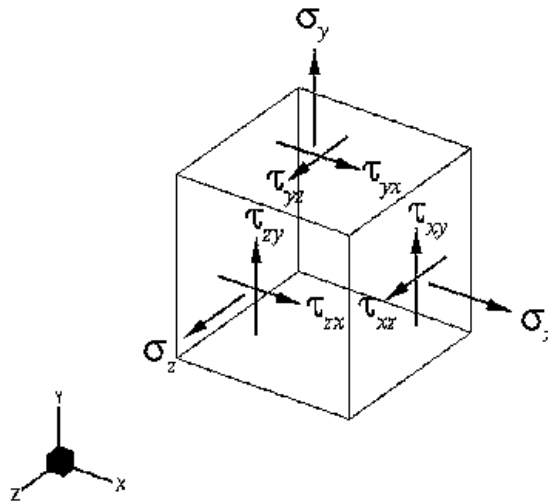


Figure 3.10: 3-D Representative Stress Volume (Timoshenko & Goodier, 1951)

3.8 Initial State

Initial state in ANSYS is the state of a structure at the start of an analysis. The common assumption is that the state of a structure is undeformed (ANSYS Inc, 2017). However, in the present study, CFRP material of the hybrid-composite unit is strained prior to the applied load.

The initial state commands allow to specify an initial stress or strain state for a given structure (ANSYS Inc, 2017). The initial state must be applied in the first load-step of the analysis.

Sample Code Specifying Initial Strain to a Material # 3

- `Inistate,set,csys,0`
- `Inistate,set,dtyp,epel`
- `Inistate,set,mat,3`
- `Inistate,define,,,,,,,,,0.0034`
- `Inistate,list`

3.9 Solution Controls

Solution controls is a collection of solution influencing functions in ANSYS, combined into one accessible menu, aimed to help designers to carry out their analysis. The following sections discuss critical solution controls used in this study.

3.9.1 Arc-Length Method

In some cases, the solution may experience convergence difficulties. The substeps may not converge via Newton-Raphson procedure by itself. If faced with a convergence difficulty, designer can utilize Arc-Length Method. This method causes the Newton-Raphson equilibrium iterations to converge along an arc

(ANSYS Inc, 2017). Figure 3.11 shows graphically the difference between Newton-Raphson method by itself versus combined with Arc-Length method.

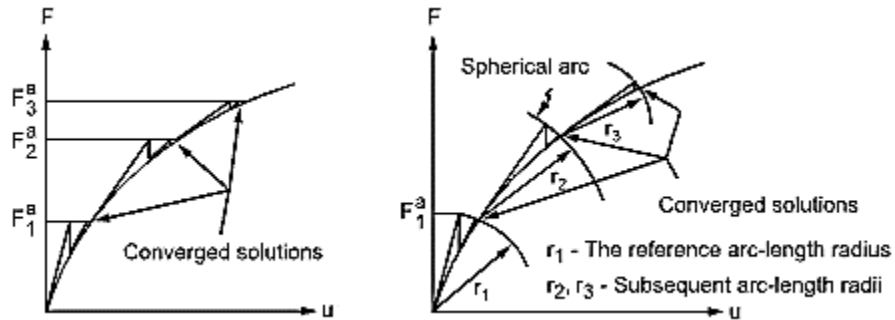


Figure 3.11: Arc-Length Method (ANSYS Inc, 2017)

ANSYS always uses designer selected elements in the first load step for all subsequent load steps regardless of which element designer may select in the following load steps. Time has another meaning if arc-length method is used during the solution. Time equals the value of time at the beginning of a load step, plus the value of the arc-length load factor (ANSYS Inc, 2017). Therefore, time is not considered a "counter" in arc-length based solutions.

3.9.2 Ramped vs Stepped Loading

Stepped loading means the same load magnitude will be applied at every substep during specific load step. However, it does not mean that loading conditions cannot be changed for the following load step. During ramped loading the load is divided equally between substeps and it cumulatively increases with every subsequent substep. The difference between ramped and stepped loading is illustrated in Figure 3.12. The value stored in KBC command sets the loading type.

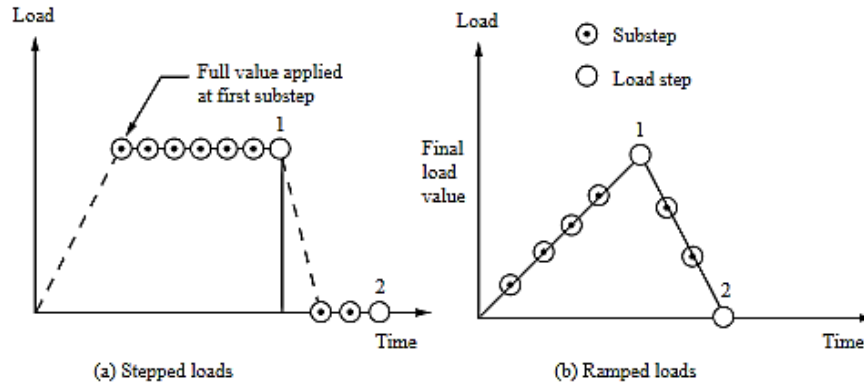


Figure 3.12: Loading Conditions (ANSYS Inc, 2017)

3.9.3 Equation Solver Selection

Analyst may select an equation solver to solve the model. By default, ANSYS uses Sparse Direct solver. However, there are two other solvers, PCG and ICG, that can suite better certain types of problems. PCG can save up to 70% of computational time when used to model 3-D solid geometries. It also includes automatic bisection function if a substep did not converge. Designers are encouraged to verify if PCG solver can be used for their model. For example, when SOLID187 elements are present in a model, PCG is permitted only for small deflection analysis.

3.10 Power vs Full Graphics

ANSYS software has two different graphics options for postprocessing: power and full graphics. Even though both options create contour plots that sometimes can look similar, the way each graphics retrieves data from the model is vastly different. For example, each graphics behaves differently at geometric, element, and material discontinuities.

When Full Graphics functions is ON, ANSYS assumes the solution is continuous. Therefore, by default the results are always averaged. Sometimes, this can lead to inaccurate results near discontinuities (Thompson & Thompson, 2017). On the other hand, when Full Graphics is OFF the program never averages nodal results across discontinuous surfaces (Thompson & Thompson, 2017). Therefore, in the present study, due to material discontinuities between all three materials, it is crucial to know this difference and to be able to assign results to the correct material.

Every analyst must be aware of the dissimilarities of the graphics options in ANSYS to exercise a good judgment. Wrong interpretation of the results will lead to wrong engineering decisions. Section 8.2 of the Mechanical APDL Basic Analysis Guide recommends always postprocessing each side of a discontinuity separately, regardless of the graphics option chosen. The present study follows this recommendation.

4 NUMERICAL MODELING OF HYBRID-COMPOSITE UNIT WITH MIX-MODE CZM USING ANSYS 17.2

4.1 Numerical Modeling

The focus of the present study is on analysis of adhesive bond between GFRP to CFRP and GFRP to concrete of the hybrid-composite unit developed by Deskovic et al. (1995). The unit is analyzed by means of finite element (FE) analysis using computer software ANSYS 17.2 Mechanical APDL (hereafter referred as ANSYS). This chapter describes steps to develop all finite element models and analysis techniques used in this study. Figure 4.1 illustrates the steps taken to develop a FE model in ANSYS. The details of application of those steps is presented in this chapter.

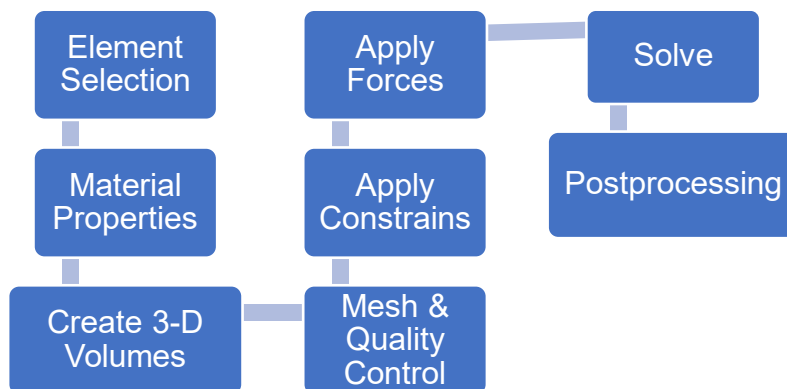


Figure 4.1: Finite Element Model Development Flow

4.2 Element Selection

4.2.1 3-D Solid Elements

All elements considered in this study are continuum solid elements. These elements provide good approximations for linear analyses and non-linear problems involving plasticity and large deformations (Da Silva & Campilho, 2012). Firstly, two most credible groups of finite elements, brick and shell elements, were chosen for the initial trials to compare their performance. These elements are also commonly used to model materials used in this study (concrete and FRP). However, elements from neither of those groups have been found to be adequate for meshing all three materials of the hybrid-composite unit. The details on this are discussed in Meshing section of this chapter.

Researchers have used Tetrahedral elements since they have been proved to be reliable. For complex geometries, it is often better to use a 10-noded tetrahedral element rather than risk having degenerate brick elements in the mesh (Thompson & Thompson, 2017). Section on Meshing provides further details on this element group. These elements with mid-side nodes utilize quadratic shape functions, which are recommended for non-linear analysis. Thus, tetrahedral elements were selected to be the elements of choice in this study. Specifically, ten-node tetrahedral element is used throughout all FEM models of this study, because it has mid-side nodes.

4.2.2 ANSYS Contact Elements

In hybrid-composite unit three materials are joined by an adhesive directly applied on a surface of each material. Thus, from the software perspective, this is a surface

to surface pair-based type of contact. Since this study analyzes the hybrid composite unit in 3-D space, TARGET170 and CONTA174 are the only contact elements that can be used to model adhesive bond between the materials (see Figure 4.2).

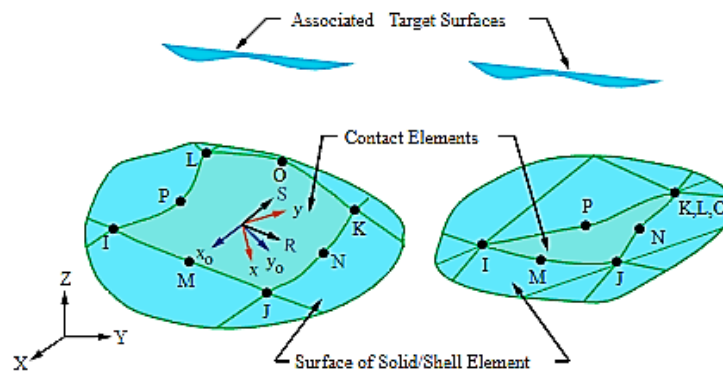


Figure 4.2: Target and Contact Elements (ANSYS Inc, 2017)

4.3 Material Models

The hybrid composite units are made of four different materials: concrete, GFRP, CFRP, and adhesive. Therefore, ANSYS model must have four material models, one for each material. Concrete and GFRP were analyzed through linear as well as non-linear material formulations in ANSYS.

4.3.1 Linear Material Models

Individual material models were defined for each material of the hybrid composite unit. Concrete and CFRP material layers were assumed to have an isotropic behavior. GFRP material layer was assumed to be orthotropic. The material properties listed in Table 4.1 are averages taken from Deskovic et al. (1995) tests on small scale hybrid composite units.

Table 4.1: Concrete, GFRP, and CFRP Material Properties (Deskovic & Triantafillou, 1995)

Symbol	Material Model 1 Concrete HS-FRC (GPa)	Material Model 2 GFRP (GPa)	Material Model 3 CFRP (GPa)
Type	Linear Isotropic	Linear Orthotropic	Linear Isotropic
E_x	19.4	20.843	80.235
E_y		8	
E_z		8	
ν_{xy}	0.2	0.33	0.35
ν_{yz}		0.1	
ν_{xz}		0.1	
G_{xy}		2	
G_{yz}		2	
G_{xz}		2	
	Material Model 1 Concrete HS-FRC (kT/mm ³)	Material Model 2 GFRP (kT/mm ³)	Material Model 3 CFRP (kT/mm ³)
Density	0.002403	1.80E-11	1.50E-12

4.3.2 Cohesive Zone Material Model

Failure mechanisms of adhesive bonding can be studied considering a) structural failure b) adhesive failure c) cohesive failure (see Figure 4.3). CZM's coupled with FE analyses is the most used method to analyze adhesive joints considering failure of an adhesive (Da Silva & Campilho, 2012). CZM model uses a combination of stress and fracture mechanics. Its application is based on continuum assumptions of thin adhesive bonds that join structural members (Campilho, Moura, & J.J.M.S., Using a Cohesive Damage Model to Predict the Tensile Behaviour of CFRP Single-Strup Repairs, 2008).

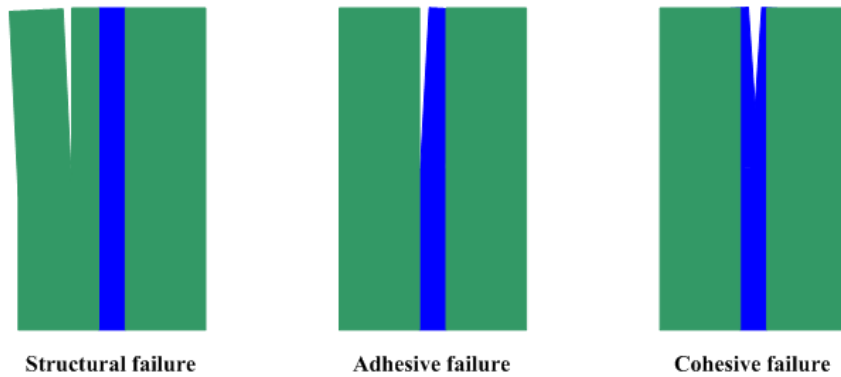


Figure 4.3: Failure Mechanisms of Adhesive Bonding

The concept of cohesive zone was proposed Barenblatt and Dugdale in early 50s through late 60s in their separate research. The technique consists of an established traction-separation laws to model interfaces or finite regions. CZM shape/laws are applied between paired nodes of contact elements representing different materials adhered together (Da Silva & Campilho, 2012). Figure 4.4 illustrates typical CZM shape and its defining variables.

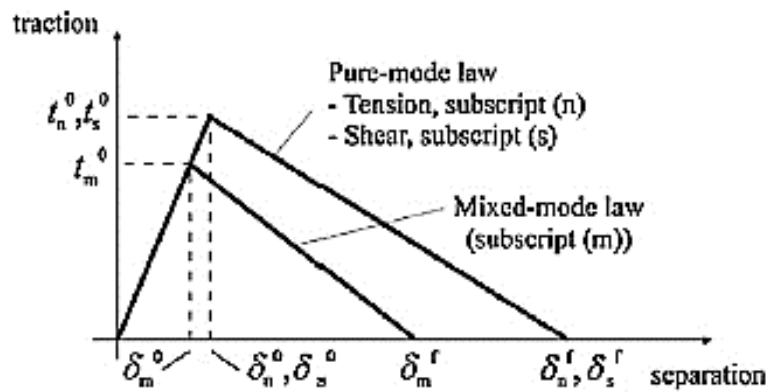


Figure 4.4: Triangular CZM Shape Laws (Da Silva & Campilho, 2012)

CZM laws distinguish between normal/tension and tangential/shear forces in the cohesive region. Thus, tension and shear in an adhesive joint may be analyzed

separately by a computer software. The subscripts n and s relate to normal and tangential forces inside of the adhesive layer respectively. The t_n and t_s present stresses at respective δ_n and δ_s displacements. The cohesive strengths, t_n^0 and t_s^0 , are the ultimate stresses that designate end of the linear and initiation of the plastic response. During plastic response crack propagates up to the adjacent set of nodes on the failure path, which allows gradual debonding between crack faces (Da Silva & Campilho, 2012). The area under the curves is the strain energy release rates G_n and G_s . The subscript m designates mix-mode, which is when both tension and shear modes of loading are analyzed simultaneously.

The triangular CZM shapes are commonly selected to model brittle adhesives that don't undergo plasticization after yielding, such as Araldite AV 138 (Da Silva & Campilho, 2012). Additionally, it was confirmed that triangular CZM shape underpredicts ductile adhesive strength, such as Araldite 2015 (Campilho, Banea, Neto, & da Silva, 2013). Therefore, both beforementioned adhesives, in this study, will be modeled using triangular shape.

The advantage of CZM is a self-propagating growth of damage without user intervention. (Da Silva & Campilho, 2012). CZM model is mesh independent since it solely relies on the interaction of the cohesive elements (Carvalho & Campilho, 2017). CZM model independently searches for damage initiation sites. However, the load increments must be sufficiently small to produce a smooth spreading damage. The cohesive strength is defined by (4.1 relating stresses and strains across the cohesive elements.

$$\begin{Bmatrix} t_n \\ t_s \end{Bmatrix} = \begin{bmatrix} K_{nn} & K_{ns} \\ K_{ns} & K_{ss} \end{bmatrix} \begin{Bmatrix} \varepsilon_n \\ \varepsilon_s \end{Bmatrix} \quad (4.1)$$

For the adhesive bonds a suitable approximation is provided by $K_{nn} = E$, $K_{ss} = G$, $K_{ns} = 0$ (Da Silva & Campilho, 2012), where E and G are the longitudinal and lateral elastic moduli respectively. The initiation of damage for mix-mode condition is specified by the quadratic nominal stress criterion given by (4.2).

$$\left\{ \frac{\langle t_n \rangle}{t_n^0} \right\}^2 + \left\{ \frac{t_s}{t_s^0} \right\}^2 = 1 \quad (4.2)$$

Where $\langle \rangle$ are the Macaulay brackets, emphasizing that a purely compressive stress does not initiate damage (Da Silva & Campilho, 2012). Complete separation is predicted by a linear power law (4.3).

$$\frac{G_n}{G_n^0} + \frac{G_s}{G_s^0} = 1 \quad (4.3)$$

To avoid convergence difficulties in FE analysis, some interpenetration between the contact elements was permitted. Studies have shown that minimum stiffness to prevent interpenetration of the crack faces without compromising the global behavior of bonded joints is $5 \cdot 10^4$ N/mm³ (Da Silva & Campilho, 2012). Implementation of line search functions and automatic stabilization algorithms has shown to obtain convergence of results. Thus, both were executed during contact analysis. Additionally, inclusion of an artificial damping coefficient must prevent divergence. According to Khoramishad et al. (2010), an appropriate damping coefficient is $\mu = 10^{-5}$ N.s/mm.

The adhesives used to model bond between concrete and FRP materials are Araldite AV138 and Araldite 2015. Both adhesives are two-component structural

epoxies that were designed to adhere dissimilar materials. Their bulk material properties are shown in Table 4.2.

Table 4.2: Bulk Material Properties of Araldite AV138 and Araldite 2015 (Carvalho & Campilho, 2017)

Property	AV138	2015
Young's modulus, E [GPa]	4.89 ± 0.81	1.85 ± 0.21
Poisson's ratio, ν	0.35 ^a	0.33 ^a
Tensile yield stress, σ_y [MPa]	36.49 ± 2.47	12.63 ± 0.61
Tensile failure strength, σ_f [MPa]	39.45 ± 3.18	21.63 ± 1.61
Tensile failure strain, ϵ_f [%]	1.21 ± 0.10	4.77 ± 0.15
Shear modulus, G [GPa]	1.56 ± 0.01	0.56 ± 0.21
Shear yield stress, τ_y [MPa]	25.1 ± 0.33	14.6 ± 1.3
Shear failure strength, τ_f [MPa]	30.2 ± 0.40	17.9 ± 1.8
Shear failure strain, γ_f [%]	7.8 ± 0.7	43.9 ± 3.4
G_{IC} [N/mm]	0.20 ^b	0.43 ± 0.02
G_{DC} [N/mm]	0.38 ^b	4.70 ± 0.34

However, it must be noted that adhesive's bulk material properties are known to be misleading and must not be used in CZM modeling (Carvalho & Campilho, 2017). Because G_n and G_s are known to depend on thickness of adhesive layer and adherends. Additionally, t_n^0 and t_s^0 do not directly relate to σ^f and τ^f , because the latter were defined without constraint effects caused by adherends (Campilho, Banea, Neto, & da Silva, 2013). Therefore, Araldite AV138 and Araldite 2015 cohesive parameters obtained thorough the direct method were used for CZM modeling in this study (see Table 4.3). Both adhesives were modeled using mix-mode debonding through triangular shape.

Table 4.3: CZM Model Properties (Carvalho & Campilho, 2017)

Cohesive Zone Material (CZM) Variables		Araldite AV138 Cohesive Law Prop.	Araldite 2015 Cohesive Law Prop.	Units
C1	maximum normal contact stress (tension)	0.0374	0.0329	GPa
C2	critical fracture energy for normal separation	0.000245	0.000533	kN/mm
C3	maximum shear stress	0.0168	0.0148	GPa
C4	critical fracture energy for tangential slip	0.00058	0.003123	kN/mm
C5	artificial damping coefficient	0.0001	0.0001	s
C6	allow tangential slip	1 (ON)	1 (ON)	

ANSYS CZM Input Commands

- TB, LAB, MAT, NTEMP, NPTS, TBOPT, EOSOPT, FuncName
 - TB, CZM, 4, 1, 6, CBDE
- TBDATA, STLOC, C1, C2, C3, C4, C5, C6
 - TBDATA, 1, C1, C2, C3, C4, C5, C6

4.4 Creation of the 3-D Model

The hybrid composite units are made by adhesion of three different materials each having different geometric shape. Therefore, from the software perspective each hybrid composite unit is made of three 3-D volumes to be later meshed with 3-D solid elements. Continuous 3-D elements suppress the approximation introduced by the plane stress or strain conditions (Da Silva & Campilho, 2012). All volumes were generated using Create and Boolean commands in ANSYS. Figure 4.5 illustrates the final 3-D model made by joining three volumes.

To simulate adhesion during non-contact analysis Boolean Glue command was used assuming a perfect bond between all three materials. Additionally, all entities were able to maintain their individual material properties, while being connected at their respective intersections. The materials comprising hybrid-composite unit are

not "added", but they become connected at their intersection (they "talk" to each other), as shown in Figure 4.6 (ANSYS Inc, 2017).

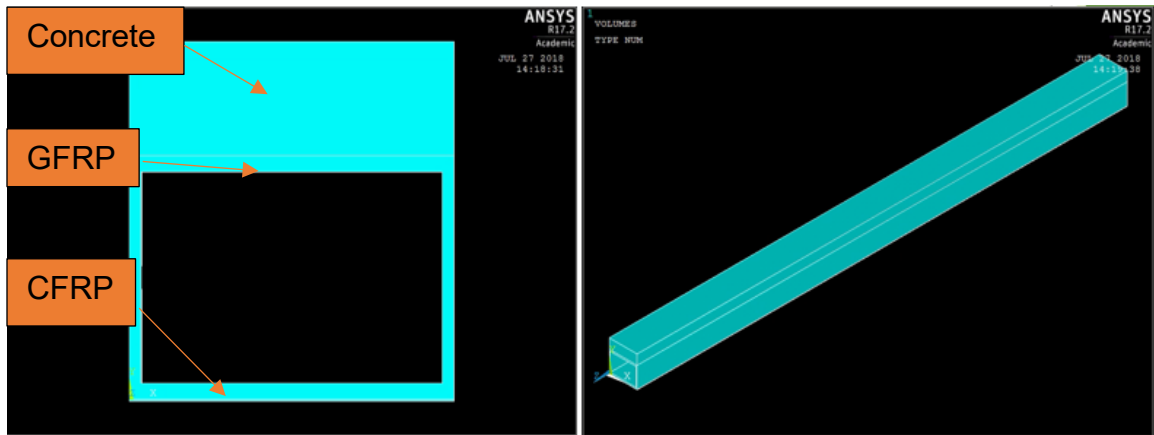


Figure 4.5: 3-D Hybrid Composite Unit in ANSYS

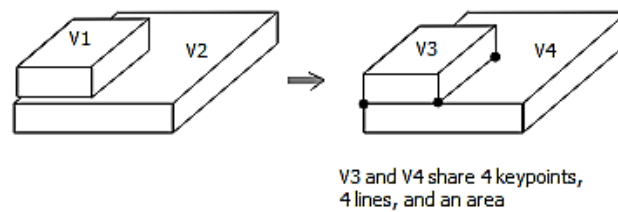


Figure 4.6: Boolean Glue Operation (ANSYS Inc, 2017)

4.5 Meshing

Shell and brick elements were considered to be the elements of choice for finite element modeling in this study. It is common to use brick elements to mesh components made of concrete and shell elements to mesh components made of composite materials. Efforts were made to mesh all three materials of the hybrid-composite unit using either of these element types. However, because of the shape of the GFRP layer (hollow box) both element types were inappropriate to mesh it without becoming degenerate. Therefore, in the present study, ten-node tetrahedral (SOLID187) is selected as the element of choice for all three layers of

the hybrid-composite unit: concrete, GFRP, and CFRP. Figure 4.7 illustrates meshed model of the hybrid-composite unit.

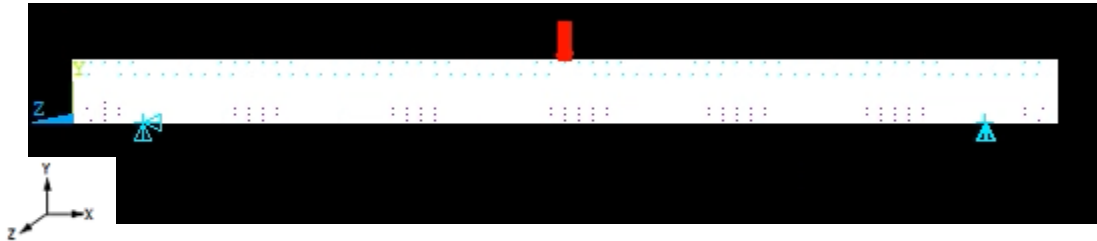


Figure 4.7: Hybrid Composite Unit Meshed Model Plot

4.5.1 Mesh Sensitivity

Mesh density is the number of finite elements per object (i.e. line, area, volume). Unfortunately, there is no rule of thumb for a suitable mesh density. In ANSYS there are several variables that control mesh density (i.e. element edge length, number of element divisions etc.). Element edge length is the parameter used to control mesh density in this study. Decreasing element edge length increases mesh density.

The procedure consists of iterations during which mesh density increases with every iteration while the applied load and constraints remain the same. With increase in mesh density, the results are expected to converge to a single value. Thus, a suitable mesh density is that at which changes in the results become negligible. Based on mesh convergence analysis performed in this study (see Figure 4.8) the appropriate element edge length for all three materials was determined to be 2 mm.

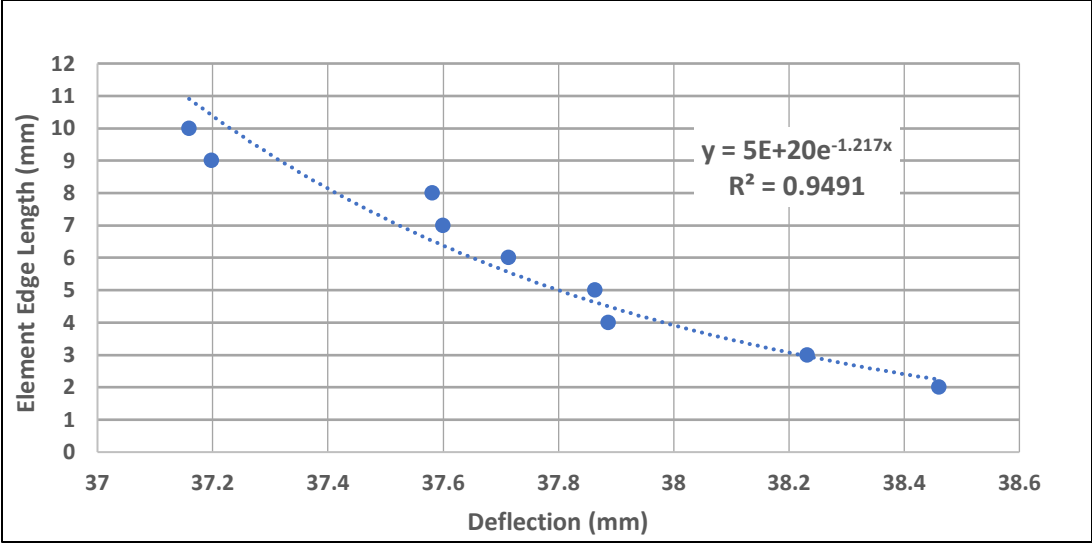


Figure 4.8: Mesh Convergence Study Plot

5 PARAMETRIC STUDIES, DISCUSSIONS, AND RESULTS

This chapter presents the analyses of adhesive bond between dissimilar materials in the hybrid-composite unit. Parameters of one of the hybrid composite units (small-scale unit #14) studied by Deskovic et al. (1995), are used to conduct numerical contact analysis. Unit #14 was chosen for this study due to its pseudo-ductile response under applied load (Deskovic & Triantafillou, 1995).

Load vs deflection graph of the unit obtained from the laboratory tests is used to validate the FE models developed in this study. Further, stresses induced in the adhesive were determined using mix-mode CZM model. The stress propagation was analyzed per load increment of 1 kN up to failure. This knowledge shall aid in design of an adhesive bond between dissimilar materials such as those considered in this study (concrete, GFRP, and CFRP).

5.1 Finite Element Modeling

The FE analysis simulates the three-point flexural test set up. This configuration exposes material's ability to resist deformation under load. The analysis also considers mix-mode fracture characterization of adhesively bonded hybrid-composite unit. To prevent the primary failure of the material due to shear stress, span to depth ratio was maintained at 16. Figure 5.1 illustrates typical response of a simply supported beam, where M , Q , and w letters stand for bending moment, shear, and deflection diagrams respectively.

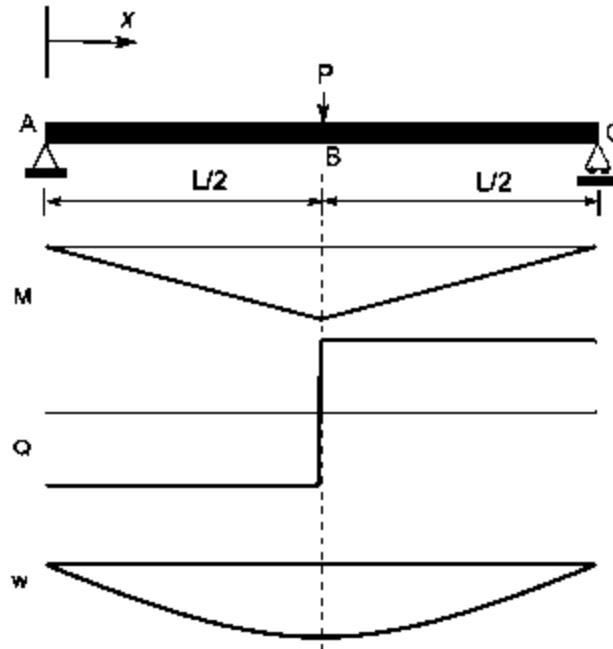


Figure 5.1: Typical Three-Point Bending Test (Google Images)

5.2 Finite Element Analysis Input

5.2.1 Implementation of Geometric Nonlinearities

All FE models of the hybrid-composite unit were solved including non-linear geometric effects. Geometric nonlinearity accounts for changes in structural stiffness due to changes in elements' shape. To activate geometric or material nonlinearity during modeling, designer must issue command NLGEOM, ON (or choose large deflections under solutions tab). The load increment was set to 1 kN per substep, for a total number of twenty-five substeps. Table 5.1 shows the solution controls for non-linear analysis (zero designates that the variable's magnitude is set to zero).

Table 5.1: Non-Linear Solution Controls

Analysis Type	Static
Analysis Options	Large Displacement Static
Time Control	Depends
Write Items to Results File	All Solution Items
Frequency	Write Every Substep
Equation Solver	Sparse Direct
Number of Restart Files	0
Frequency	Write Every Nth Substep
Line Search	Prog Chosen
DOF Solution Predictor	Prog Chosen
VT Speedup	Off
Maximum Number of Iterations	Prog Chosen
Creep Option	No
Equivalent Plastic Strain	0.15
Explicit Creep Ratio	0.1
Implicit Creep Ratio	0
Incremental Displacement	1000000
Points Per Cycle	13
Cutback According to Predicted Number of Iteration	Yes
Always Iterate to 25 Equilibrium Iteration	No
Program Behavior Upon Nonconvergence	Terminate but Do Not Exist
Activated Arc-Length Method	No
Max Multiplier	0
Min Multiplier	0
Arc-Length Termination	No
Displacement Limit	0
Stabilization	Constant Stabilization
Control	Energy Dissipation
Value	0

5.2.2 Implementation of Contact Elements

In contact analyses the adhesive bond is analyzed through a pair of contact elements: target and contact. Each of those elements has its own settings. Those are defined as input prior to issuing Solve command in ANSYS. According to ANSYS Contact Technology Guide, best-practices settings for each contact

element were established for the given condition. Table 5.2 through Table 5.4 summarize all the settings set for the contact elements in this study. When zero is listed in value column the setting is set to default.

Table 5.2: Contact Element Key Options Settings

Key Options Used	Value	Definition
1 (Select Degrees of Freedom)	0	UX, UY, UZ
2 (Contact Algorithm)	0	Augmented Lagrangian
3 (Units of Normal Contact Stiffness)	0	(Force/Length ³)
4 (Contact Detection)	0	(On Gauss Points)
5 (C_{nof}/I_{cont} Automated Adjustment)	4	default Auto ICONT
6 (Contact Stiffness Variation)	0	Use default range
7 (Time Incrementation Control)	0	No control
8 (Asymmetric Contact Selection)	0	No action
9 (Effect of Initial Penetration)	Ignored During Always Bonded Analysis	
10 (Contact Stiffness Update)	2	Each Iteration Based on Current Mean Stress of Underlying Elements
11 (Shell Thickness Effect)	0	Exclude
12 (Behavior of Contact Surface)	5.00	Always Bonded

Table 5.3: Target Element Settings

Target Element		
Constants Used	Value	Comment
R1	-	-
R2	-	-
Key Options Used	Value	Definition
1 (Element Order)	1	High Order Elements
2 (Boundary Conditions for Rigid Target Nodes)	0	Automatically Constrained by The Program
3 (Behavior of Thermal Contact Surface)	1	Treated as Free-Surface
4 (DOF Set to be Constraints)	Not Used in Bonded Surface to Surface Contact	
5 (MPC Constraints)	Not Used in Bonded Surface to Surface Contact	
6 (Symmetry of a Constrained Surface)	Not Used in Bonded Surface to Surface Contact	

Table 5.4: Contact Analysis Solution Controls

Contact Analysis Solution Controls	
Time Step Size/Number of Substeps	25
Newton-Raphson Option	FULL
Adaptive Descend	OFF
Unsymmetrical Solver	OFF
Line Search	ON
Predictor-Corrector	ON
NLHIST Command	ON

5.2.3 Failure Sequence (Strain Failure Criteria)

As previously discussed, ANSYS strain failure criteria function will be used to determine failure sequence of each material of the hybrid-composite unit. Table 5.5 list failure strain magnitudes of each material. These ultimate strain values used in the study are based on those reported in Deskovic et al.

Table 5.5: Ultimate Strain Values (Deskovic & Triantafillou, 1995)

Material	Failure Strain %	Failure Strain	Initial Strain Small Scale Unit 14
Normal Concrete	0.38%	0.0038	
HS-FRC Concrete	0.50%	0.0050	
GFRP Small Scale	1.717%	0.01717	
GFRP Large Scale	see page 218		
G/CFRP	1.150%	0.0115	0.0034
CFRP	1.050%	0.0105	

5.2.4 Initial Strain

The experiment carried out by Deskovic et al. (1995) included prestressed CFRP bonded with the hybrid-composite unit. The ANSYS initial strain commands have been used to model the prestress of CFRP layer. To incorporate the initial strain into the analysis, load step files were created in a separate folder. Commands to set initial strain and create load step files are listed below.

ANSYS Initial Strain Commands

- Inistate, set, csys, 0
- Inistate, set, dtyp, epel
- Inistate, set, mat, 3
- Inistate, define,,,,,,,,,0.0034
- Inistate, list

Commands to Create Load Step Files

- Write to file – load step 1 (only initial strain is applied)
- Solve
- Write to file – load step 2 (only concentrated load is applied)
- Solve from LS files
- Starting LS # 1, Ending LS # 2, Increment 1

5.3 Finite Element Model Verification

To insure accuracy of the results, every model has been verified for absence of errors prior to solution. Conveniently for the analyst, ANSYS creates an error-log file, where it records all the error and warning messages produced since the first creation of the database file. The goal of the error-log file is to secure the accuracy of the results.

At the end of each FE solution in this study error-log file had been reviewed. No errors have been written for FE models referenced in this study. Some models had warning messages recorded into their error-log files due to shape testing violations. It is important to mention that warning messages have not been proven to be harmful to the solution (Thompson & Thompson, 2017). On the other hand, error messages have significant effect on the accuracy of the results.

In general, shape testing looks at the geometrical properties of every individual element in a given mesh. If some of the elements' geometric properties are not

within the default boundaries, shape testing warning message is written into the error-log file. Examples of geometric properties that shape testing assesses are: deviation from the parallel state, maximum angle in the element, element Jacobian ratio, and element warping factor. Overall, different types of elements are checked against different geometric requirements.

Overall, shape testing had revealed that some of the elements of CFRP layer violated shape warning limits. Less than 5% of CFRP elements had at least one angle less than 2.5 degrees (see Figure 3.3). Unfortunately, this was inevitable condition due to CFRP layer thickness set to 0.3 millimeters. Thus, CFRP layer was too thin and some of the mesh elements had to be stretched to fill in the volume. No other error nor warning messages were listed in all error-log files reviewed in this study.

5.4 Finite Element Model Validation

This section validates that the FE models used in this study were comparable to hybrid-composite unit #14. Figure 5.2 shows the result of the experimental work on unit #14. The failure sequence and load vs displacement graph are both represented by the dashed line and callouts respectively. This graph was analyzed and compared with the load vs displacement graph predicted by FE model used in this study (see Figure 5.3). Failure sequence was used to compare failure sequence from the FE model with that reported by Deskovic and Trintafillou (1995) in Figure 5.2. Further strain distribution across the depth, and variation of the neutral axis were extrapolated from the FE model and compared with Deskovic et al. (1995) theoretical predictions.

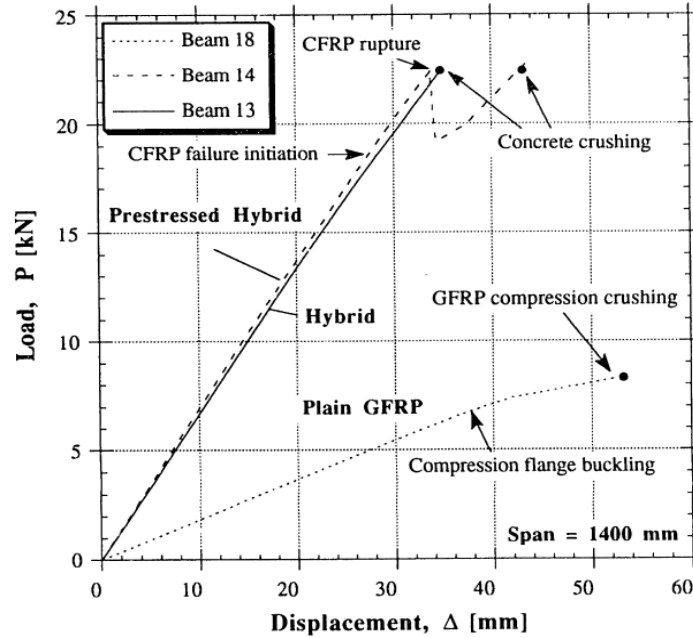


Figure 5.2 Load vs Displacement Unit # 14 (dashed line) (Deskovic & Triantafillou, 1995)

The hybrid-composite unit # 14 had typically a linear relationship between applied load and displacement (see Figure 5.2). Further, the unit had failed at $P = 22.5$ kN with the corresponding displacement of 34 mm. The slope of the graph up to the point of failure is 0.66176 kN/mm. The load vs displacement graph in Figure 5.3 is based on the FE model of unit #14. The slope of this curve is 0.6637 kN/mm, which compares well with that reported by Deskovic et al. (1995).

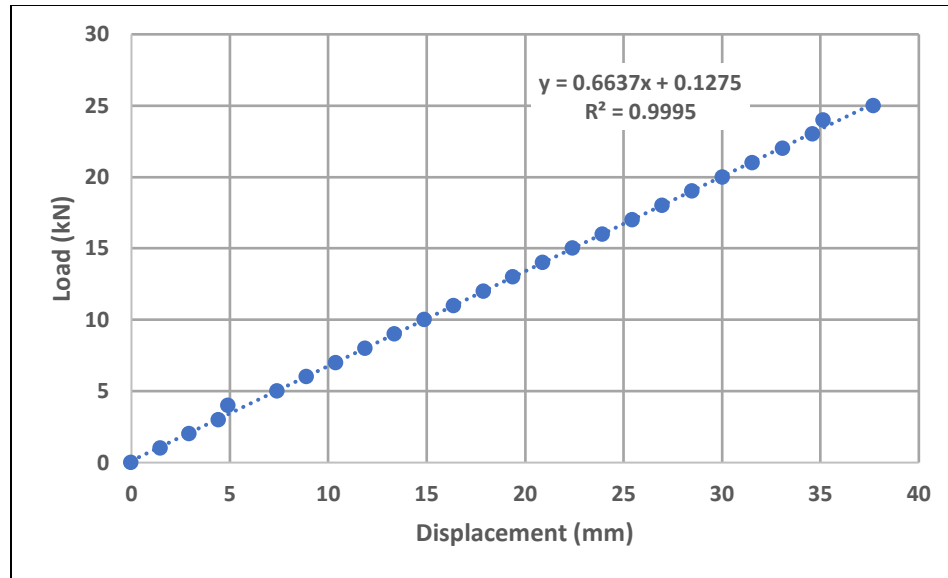


Figure 5.3: Load vs Displacement of Unit # 14 FEA Model in ANSYS

Figure 5.4 illustrates the deformed shape of the hybrid-composite unit after full load was applied during three-point-bending test in FE model. The FE model had predicted vertical displacement of 30.1429 mm at $P = 22.5$ kN, which compares well with that reported by Deskovic et al.

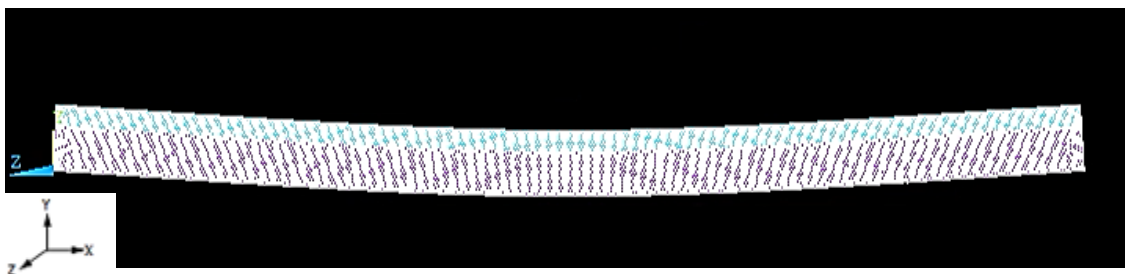


Figure 5.4: Elevation View of the Deformed Hybrid-Composite Unit

Figure 5.5 and Figure 5.6 illustrate induced stresses in the hybrid-composite unit. Per best-practices, the stress contours are continuous, which is an indication that element mesh density is within an acceptable size. Additionally, the top and bottom fibers of the FE model is in compression and tension respectively, under three-

point-bending test. Thus, a good correlation was observed between the results from physical laboratory test and the FE model.

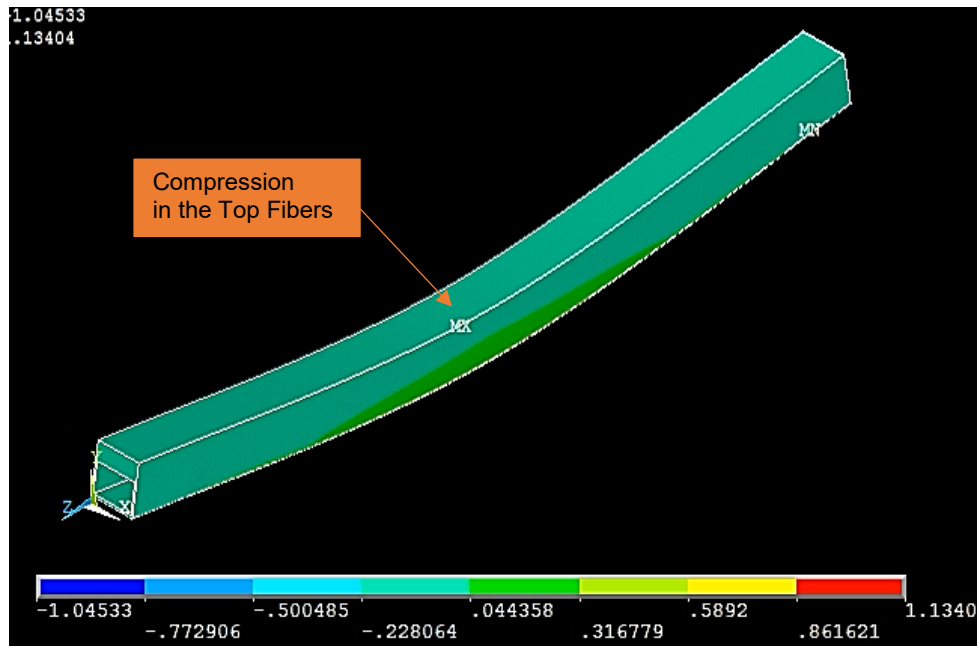


Figure 5.5: Top Isometric View of the Hybrid-Composite Unit During FE Modeling

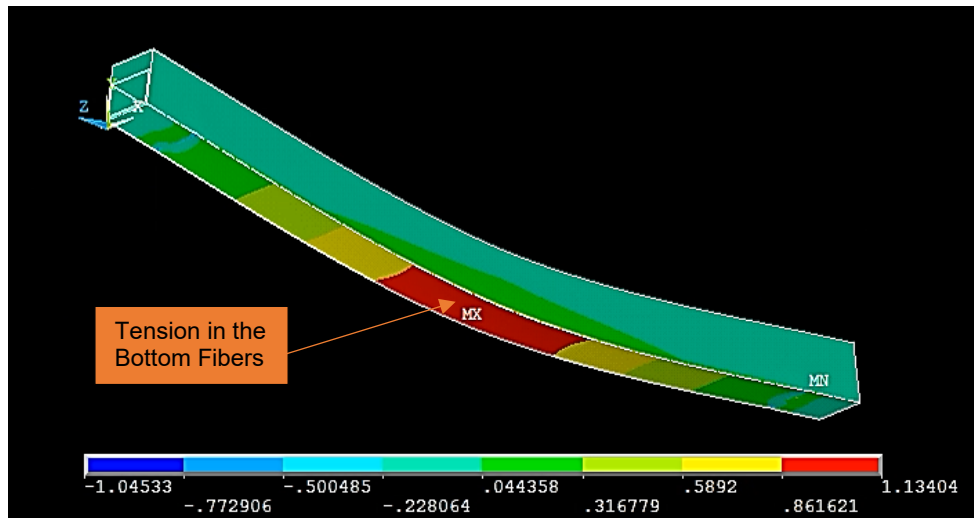


Figure 5.6: Bottom Isometric View of the Hybrid Composite Unit During FE Modeling

According to Figure 5.7, CFRP layer failure, of unit #14, initiated at $P = 18$ kN (see Figure 5.2). Based on the FE analysis, the results agree with the reported

experimental value. A material is considered to have failed when its Failure Index, I_F , is equal to one. Figure 5.7 shows CFRP layer Failure Index to be between 0.83 and 0.99 at $P = 18$ kN (mustard color). Thus, failure is shown to be initiating at the same load as it was reported by laboratory experiment. This is an excellent agreement with the reported failure sequence during the actual physical test.

Further, Figure 5.2 illustrates that the CFRP layer failed at $P = 22.5$ kN followed by the concrete failure also at $P=22.5$ kN, with an increase in displacement.

The FE analysis results are in good agreement with this sequence and the ultimate failure load magnitude. Figure 5.8 illustrates complete failure of the CFRP layer at $P = 22$ kN followed by complete concrete failure at $P = 23$ kN illustrated in Figure 5.9. Thus, FE model was able to predict the failure sequence of the real three-point bending test.

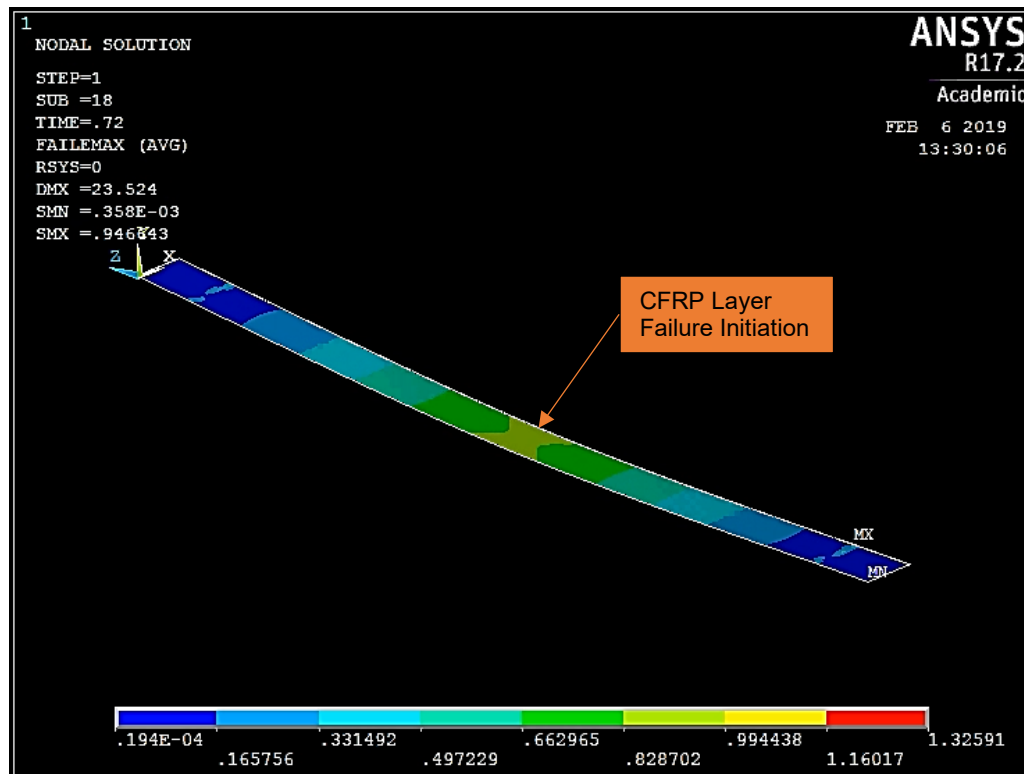


Figure 5.7: CFRP Layer Failure Initiation

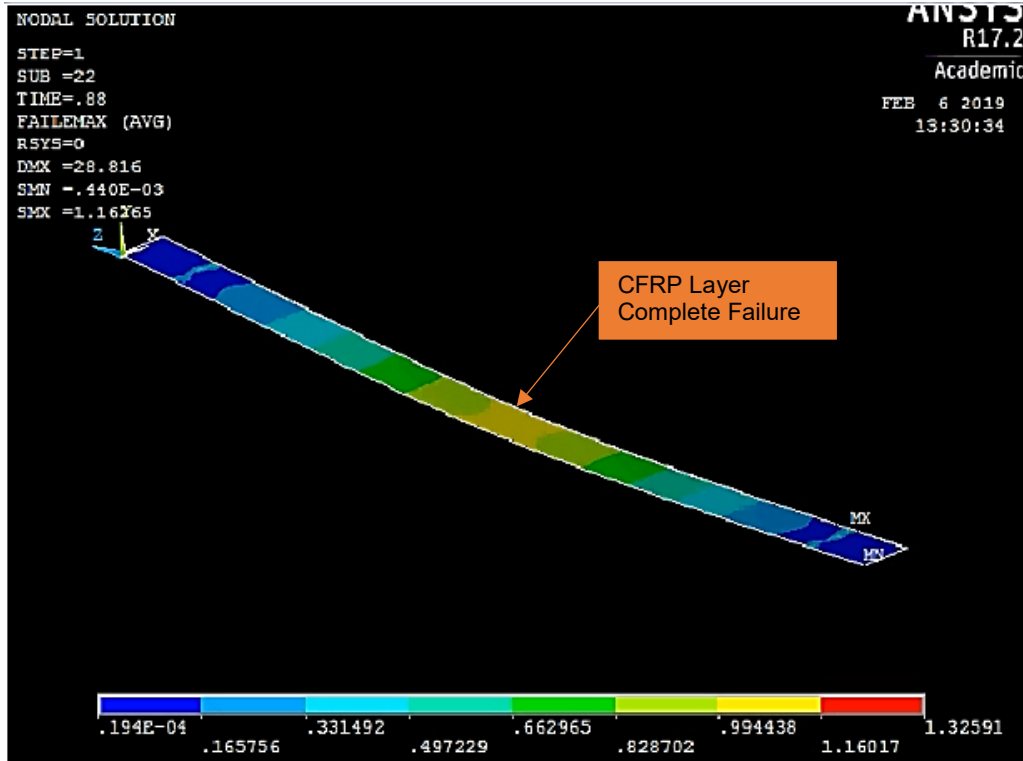


Figure 5.8:CFRP Layer Complete Failure

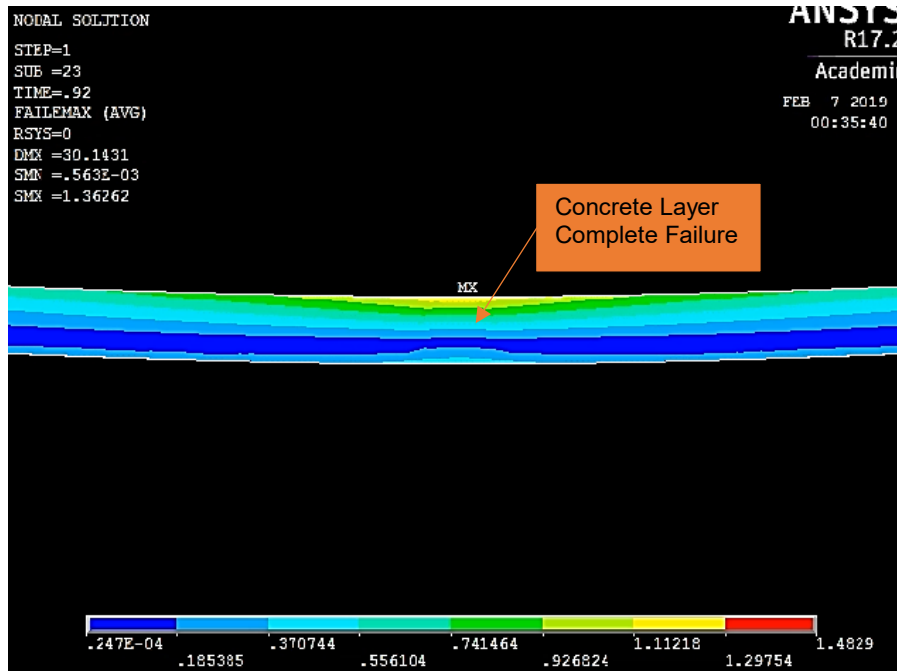


Figure 5.9: Concrete Layer Complete Failure Elevation View

According to Deskovic et al. (1995) predictions, the neutral axis of a hybrid composite unit is expected to be relatively close to the concrete-GFRP interface. As a matter of fact, the strain distribution of hybrid unit #14 from the FE analysis has shown that indeed the neutral axis is at the bottom of the concrete layer (see Figure 5.10).

Based on the information discussed previously, the FE model of unit #14 is in good agreement with the results reported by Deskovic et al. (1995). Section 5.5 presents results on the adhesive bond between dissimilar materials. Specifically, discussions are made on the stresses in adhesive layers between concrete and GFRP as well as GFRP and CFRP.

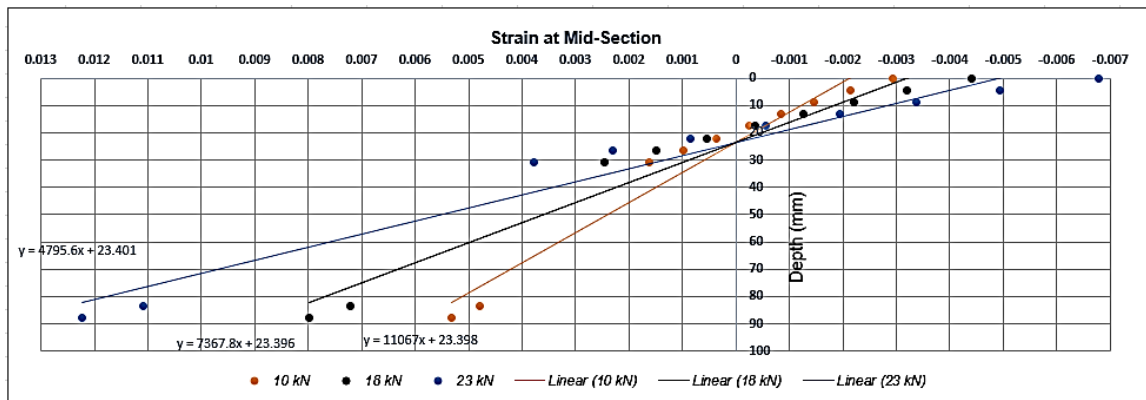


Figure 5.10: Average Strain Distribution Per Loadstep

5.5 Adhesive Contact Analysis

Due to increasing need for lightweight structures, adhesive joining is becoming more common in civil engineering. Other industries have already adopted adhesive bonding decades prior. For example, today's average per automobile consumption of adhesives is 20 kg. Additionally, Boeing 787 and Airbus A350 contains more

than 50% of bonded components (He, 2011). This section presents results of the FE contact element analysis in ANSYS between dissimilar materials of the hybrid-composite unit. The stresses in adhesive layers between concrete and GFRP as well as GFRP and CFRP were analyzed using two mix-mode CZM models of adhesives listed in Table 4.3.

The three-point-bending test was used as the loading mechanism during the FE contact analysis. It was determined that three-point bending of a single-lap joint (see Figure 5.11) and single-lap joint subjected to tension induce the same effect in an adhesive. Both introduce large bending moments along the external edge of the overlap (see Figure 5.12) (Grant, Adams, & da Silva, 2010). Thus, high stress concentrations are expected along the external edge of each adhesive.

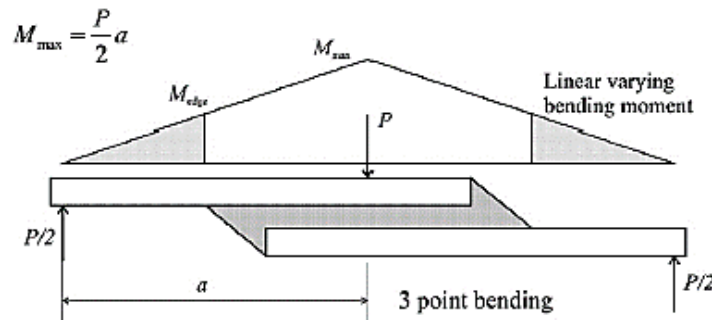


Figure 5.11: Single-Lap Joint During Three Point Bending (Grant, Adams, & da Silva, 2010)

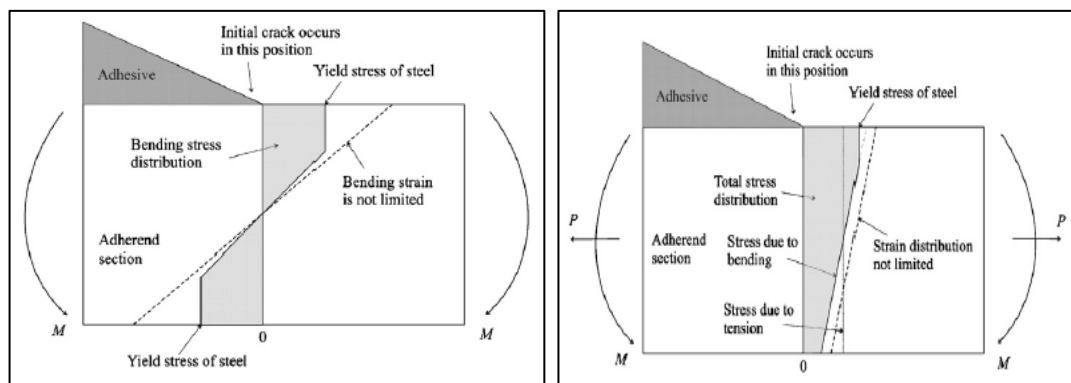


Figure 5.12: Joint Under Three-Point Bending (left) and Joint Under Tension (right) (Grant, Adams, & da Silva, 2010)

The contact analysis is highly non-linear and requires significant computational resources; therefore, the study utilized symmetry about the longitudinal axis of the hybrid-composite unit. Only half of unit #14 was modeled in ANSYS. To model symmetry during the contact analysis, out-of-plane rotations and displacements in longitudinal direction were fixed (see Figure 5.13 and Figure 5.14).

Stress concentrations are common at the edges of the overlap in the adhesively bonded joints. These originate due to uneven straining of the adherends (shear stress concentration) and eccentricity of the applied load (peel stress concentration) (Campilho, Banea, Neto, & da Silva, 2013). These stresses are ultimately responsible for the failure of the joint (He, 2011). The stress distribution in the joint is primarily controlled by the geometry and materials of the adherends and adhesives (Kumar & Pandey, 2010).

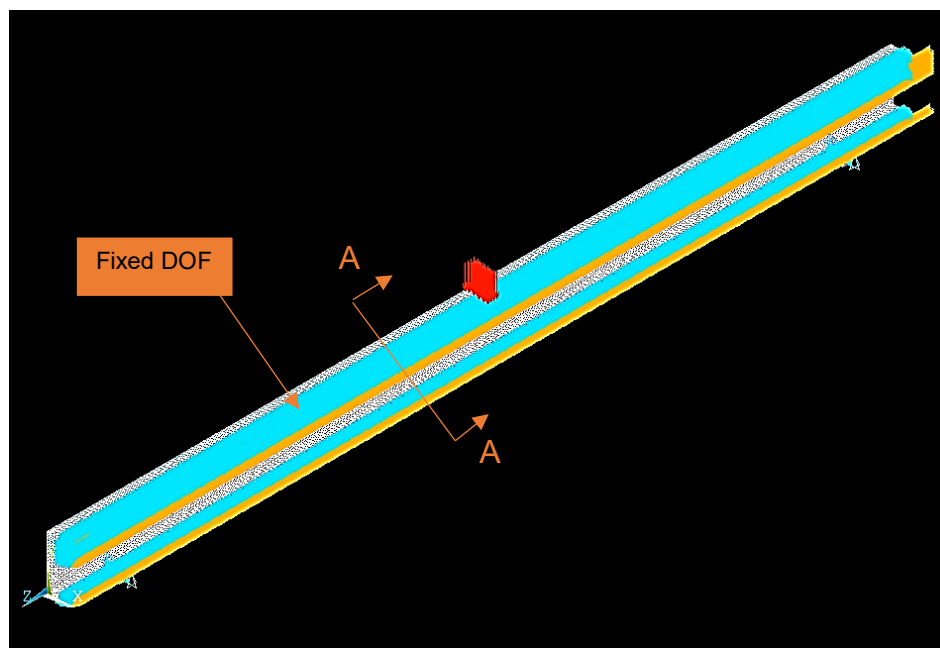


Figure 5.13: Iso View of Half Hybrid-Composite Unit with Constrained Degrees of Freedom During Contact Analyses

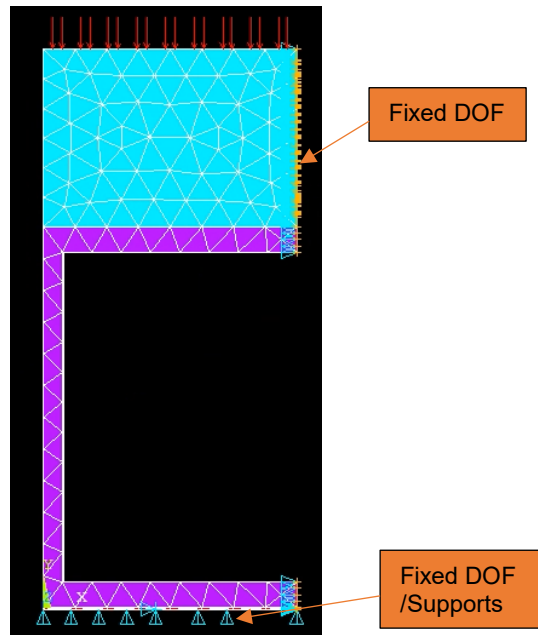


Figure 5.14: Cross-Section A-A View of Hybrid-Composite Unit with Constrained Degrees of Freedom During Contact Analyses

Therefore, adhesive joints must be designed to minimize stress concentrations to increase overall joint strength. Number of studies were focused on modification of the geometry of the adherends, adhesives, or the overlap area. However, the overall geometry of the joint is usually dictated by complexities of manufacturing (Kumar & Pandey, 2010).

Others investigated effects of Young's modulus, E , of adhesives on stress distribution in the bondline. Those studies concluded that adhesives with smaller values of E result in more uniform stress distribution with lower peak stresses (Carvalho & Campilho, 2017). In other words, decrease in adhesive stiffness decreases the peak stresses (Kumar & Pandey, 2010). Thus, the failure mechanism in adhesive joints is highly dependent on the ductility of the adhesive

(Carvalho & Campilho, 2017). Yet, the peak strains in an adhesive do not follow this conclusion. They will remain high and as a matter of fact will be noticeably higher for ductile adhesives (Kumar & Pandey, 2010).

The latter is not a concern for joints bonded with ductile adhesives over large overlap areas; as long as there is enough ductility in the adhesive to carry the load even after its ultimate strength was reached (Carvalho & Campilho, 2017). On the other hand, in the case of a joint bonded with brittle adhesive, the joint will fail when adhesive strength is attained anywhere in the bondline (Campilho, Banea, Neto, & da Silva, 2013). Figure 5.15 demonstrates these concepts through experimental work completed by Carvalho et al. (2017) P_m is the ultimate carrying load by the single-lap joint and L_o is the overlap length.

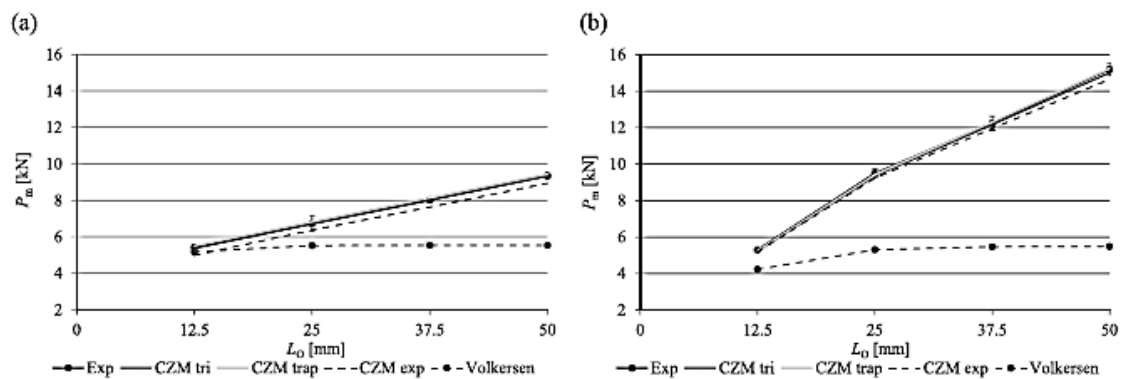


Figure 5.15: Experimental, Analytical, and Numerical $P_m - L_o$ Curves Considering Triangular, Trapezoidal, and Linear-Exponential CZM Laws Araldite AV138 (a) and Araldite 2015 (b) (Carvalho & Campilho, 2017)

From previous discussions, it was expected that the shear stresses would be maximum at the edges and decrease towards the interior of the adhesive (Kadam, Firake, & Pawar, 2015). Overall, the FE contact analysis results agree well with this prediction. However, contact analysis revealed a complex 3-D state of stress

for both adhesives (Araldite AV 138 and Araldite 2015). This distribution is similar to the one observed by Kumar et al.,2010 in the 3-D FE analysis of a single-lap joint. The highest stresses in normal and lateral directions were still located at the external edge. The normal stress in concrete-GFRP and GFRP-CFRP bondlines was controlling the failure per quadratic nominal stress criterion (see (4.2)).

5.5.1 Concrete-GFRP Adhesive Bond Interface

Figure 5.16 illustrates Araldite 2015 3-D state of shear stress between concrete and GFRP materials of the hybrid-composite unit. Similar shear stress distribution was observed for Araldite AV 138. The high stress concentrations are located along the external edge of the overlap increasing toward the center of the unit. In the same time, due to the 3-D state of stress, shear stresses are decreasing in lateral direction towards the interior of the adhesive bondline (see Figure 5.17 and Figure 5.18).

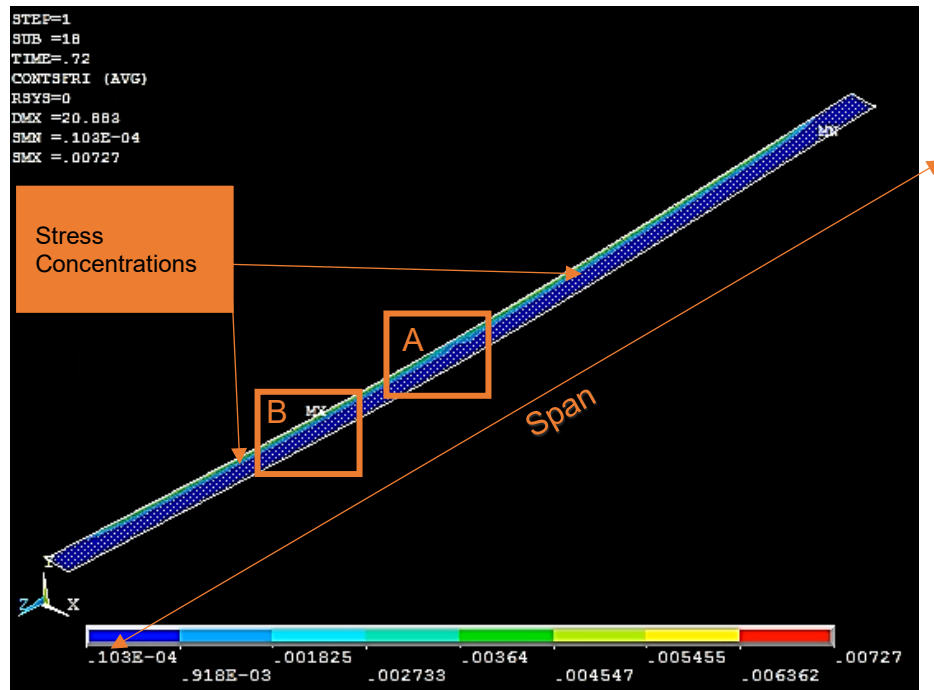


Figure 5.16: Concrete-GFRP Adhesive Shear Stress Distribution Contour Plot (Araldite 2015)

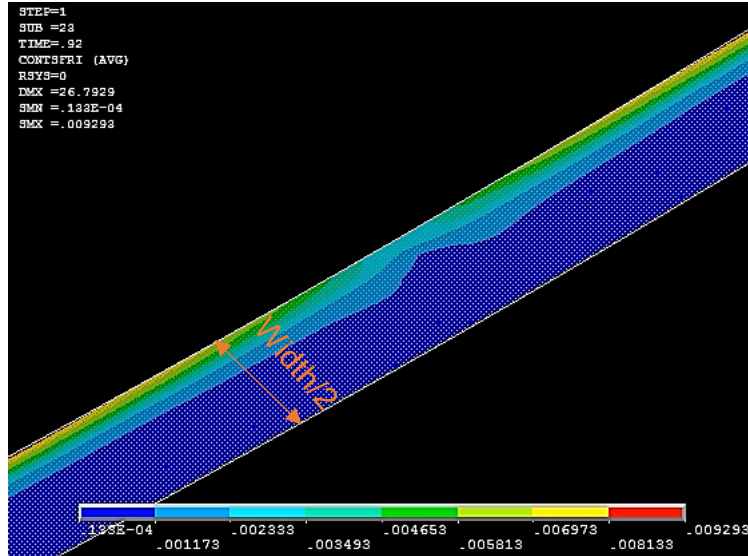


Figure 5.17: Sector A) Concrete-GFRP Adhesive Shear Stress Distribution Contour Plot (Araldite 2015)

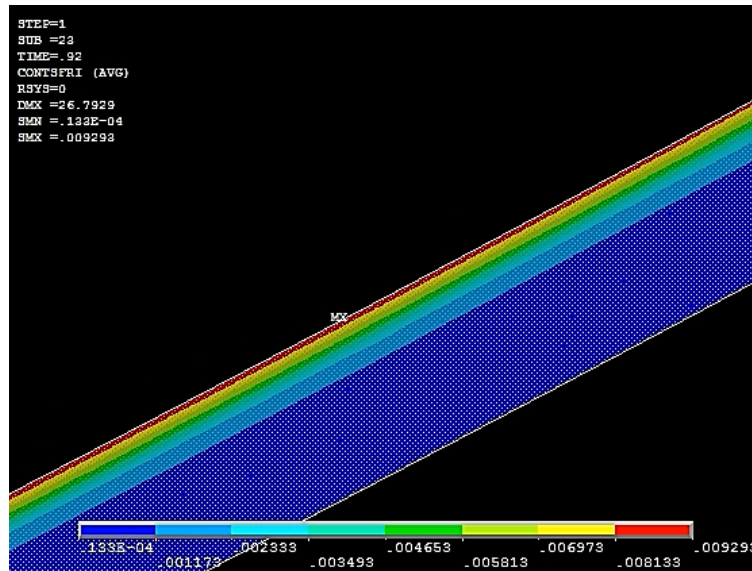


Figure 5.18: Sector B) Concrete-GFRP Adhesive Shear Stress Distribution Contour Plot (Araldite 2015)

All stress distributions of both adhesives presented in this study were normalized against the average shear stress ($\tau_{avg} = 4.61 \cdot 10^{-3}$ GPa). Figure 5.19 compares the stress concentration along the external edge of the bondline in Araldite AV138

versus those in Araldite 2015. According to the predictions, due to its ductile characteristics, Araldite 2015 experienced lower shear stress concentrations than more brittle Araldite AV138. Figure 5.20 further supports this observation. It illustrates that shear stresses indeed are decreasing in lateral direction towards the interior of the adhesive bondline.

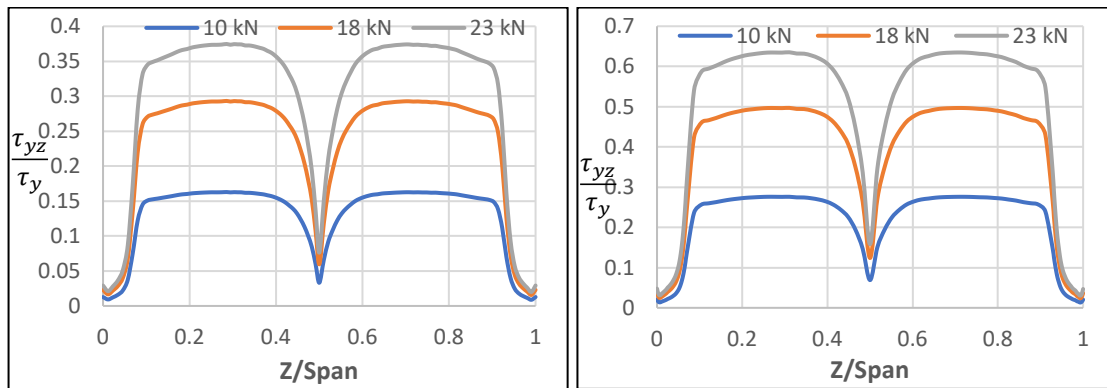


Figure 5.19: Concrete-GFRP Adhesive External Edge Longitudinal Shear Stress Distribution Araldite AV 138 (left) vs Araldite 2015 (right)

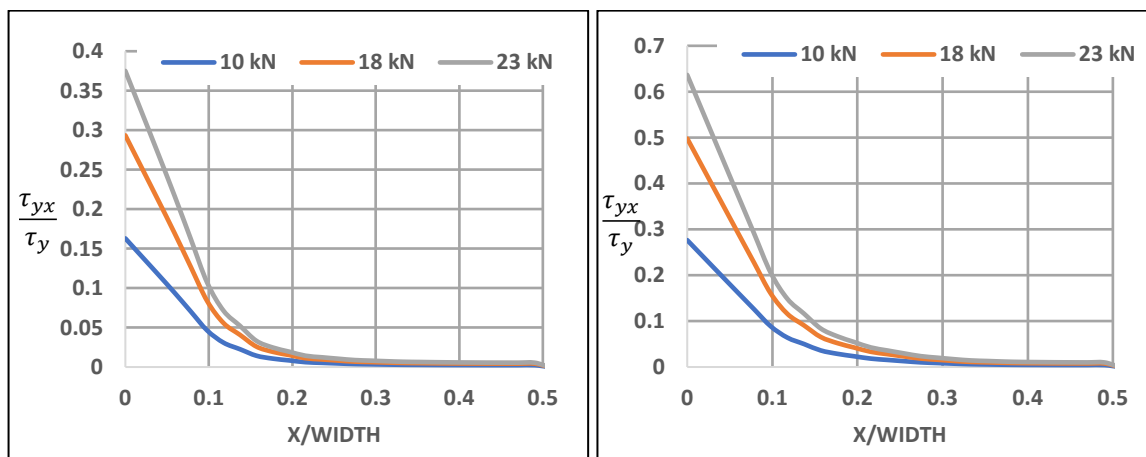


Figure 5.20: Concrete-GFRP Adhesive Lateral Shear Stress Distribution at 1/3 of the Span Araldite AV 138 (left) vs Araldite 2015 (right)

Figure 5.21 illustrates Araldite 2015 3-D normal stress distribution between concrete and GFRP materials of the hybrid-composite unit. The shear stress distribution Araldite 2015 was similar to that observed for Araldite AV 138. The high normal stress concentrations were detected along the external edge of the overlap. Contrary to shear stresses, normal stress concentrations are localized near the supports and center of the specimen. In the same time, due to the 3-D state of stress, normal stresses are decreasing in lateral direction towards the interior of the adhesive bondline (see Figure 5.22 and Figure 5.23).

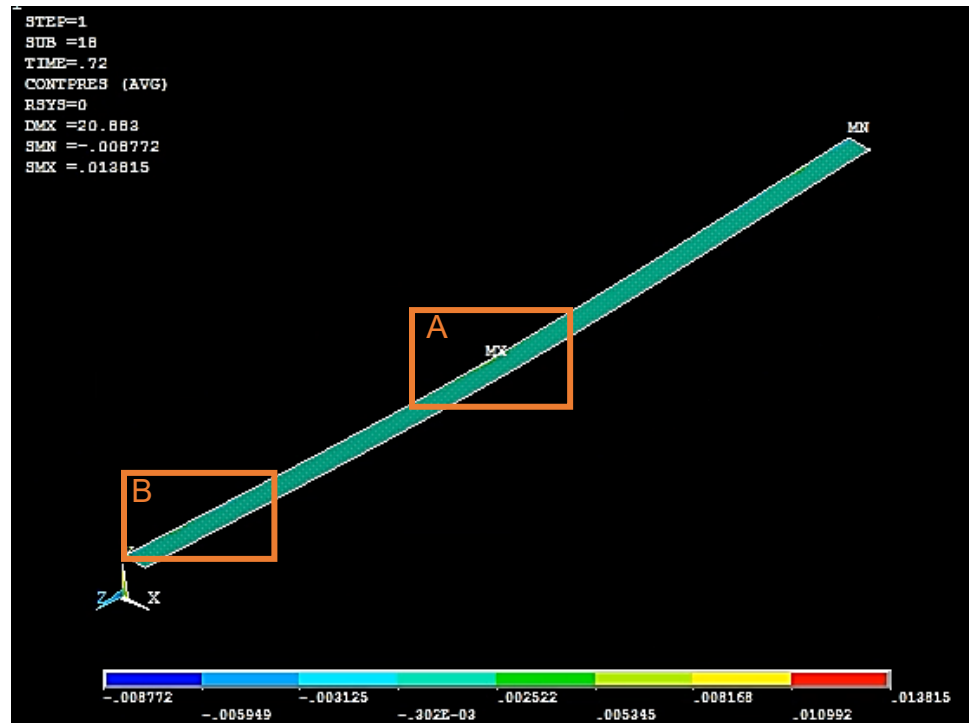


Figure 5.21: Concrete - GFRP Adhesive Normal Stress Distribution Contour Plot (Araldite 2015)

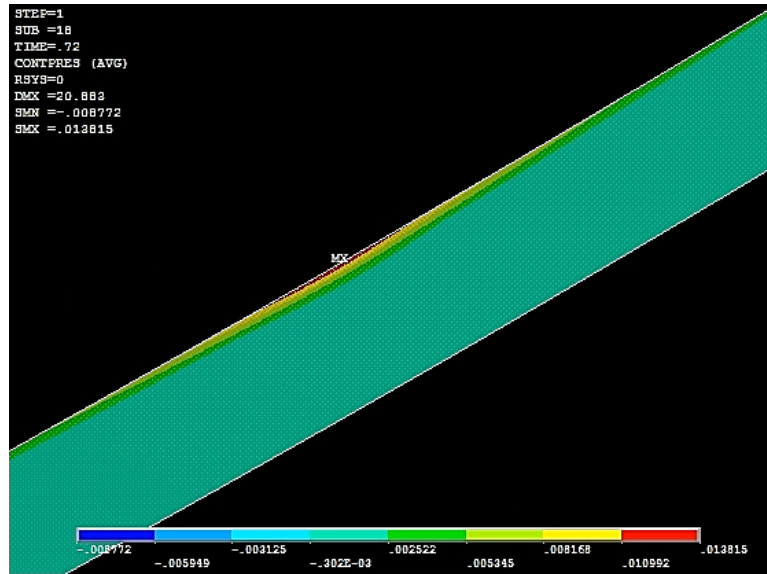


Figure 5.22: Sector A) Concrete - GFRP Adhesive Normal Stress Distribution Contour Plot (Araldite 2015)

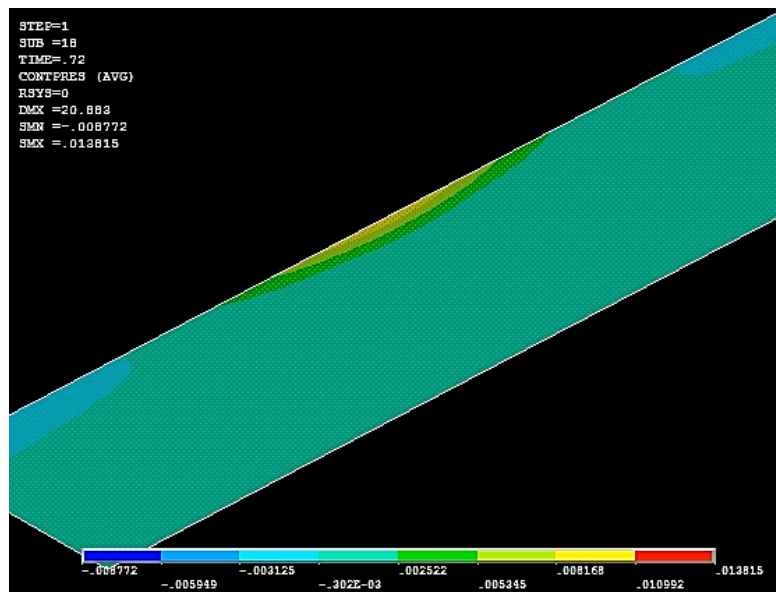


Figure 5.23: Sector B) Concrete - GFRP Adhesive Normal Stress Distribution Contour Plot (Araldite 2015)

The normal stresses concentrations observed in Araldite AV138 were higher than in Araldite 2015 (see Figure 5.24). In both adhesives, the highest normal stress concentrations were detected at the center of the span. Figure 5.25 illustrates that

normal stresses, similar to the shear stresses, are decreasing in lateral direction towards the interior of the adhesive bondline.

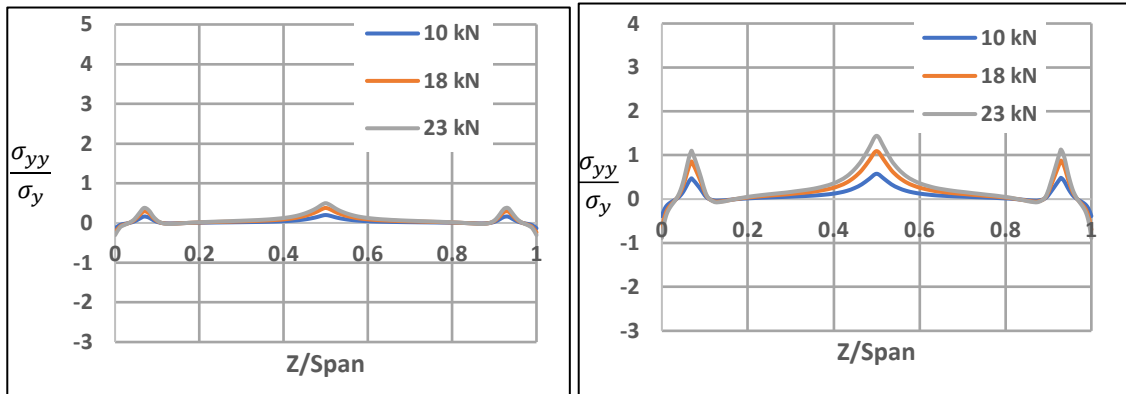


Figure 5.24: Concrete – GFRP Adhesive Layer External Edge Longitudinal Normal Stress Distribution Araldite AV 138 (left) vs Araldite 2015 (right)

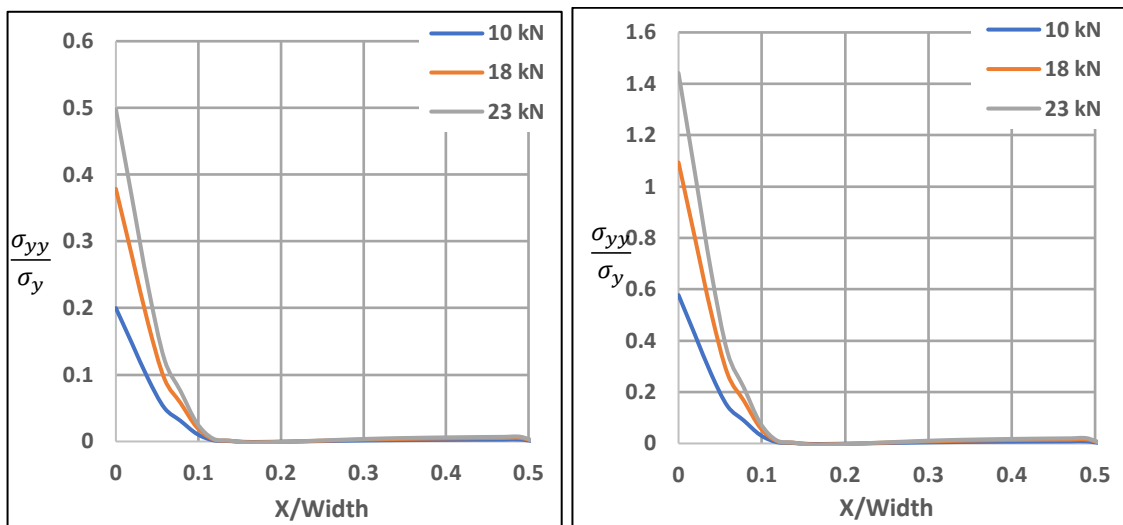


Figure 5.25: Concrete – GFRP Adhesive Lateral Normal Stress Distribution at the Center of the Unit Araldite AV 138 (left) vs Araldite 2015 (right)

5.5.2 GFRP-CFRP Adhesive Bond Interface

Figure 5.26 illustrates Araldite 2015 3-D shear stress distribution between GFRP and CFRP materials of the hybrid-composite unit. Similar shear stress distribution was observed for Araldite AV 138. Figure 5.26 illustrates shear stress concentrations located along the external edge with the extremely high values near

the supports. The peak shear stresses at the supports are due to the combination of the expected edge shear stress concentrations and additional lateral shear stresses concentrations produced by the constraint from the supports. The constrained condition of the supports introduces additional uneven strains on each side of the supports. Thus, additional lateral shear stress concentrations are produced on each side of the supports. The shear stresses at the supports are decreasing in lateral direction towards the interior of the adhesive bondline (see Figure 5.27 and Figure 5.28).

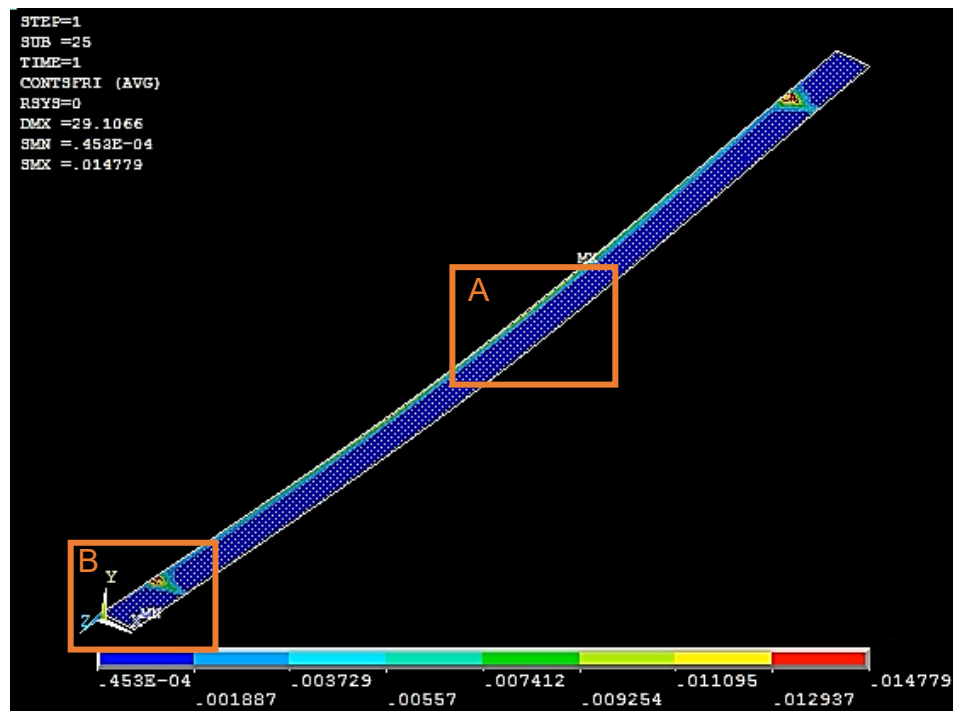


Figure 5.26: GFRP – CFRP Adhesive Shear Stress Distribution Contour Plot (Araldite 2015)

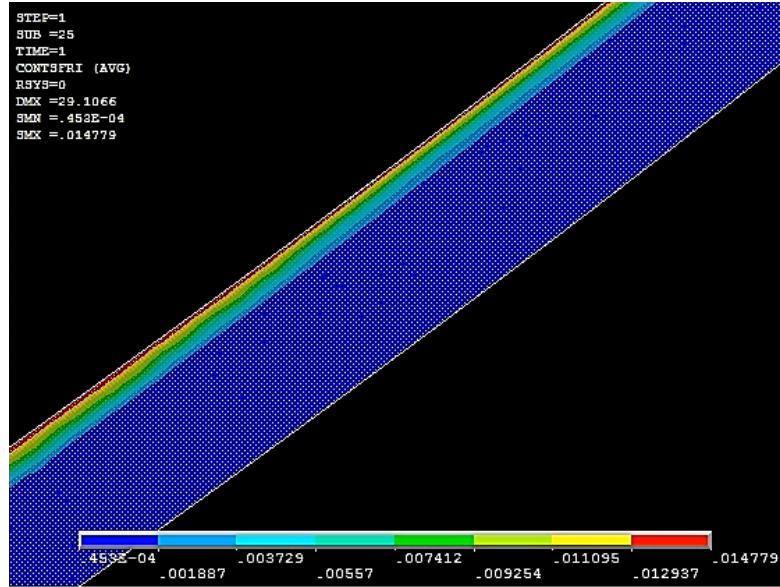


Figure 5.27: Sector A) GFRP – CFRP Adhesive Shear Stress Distribution Contour Plot (Araldite 2015)

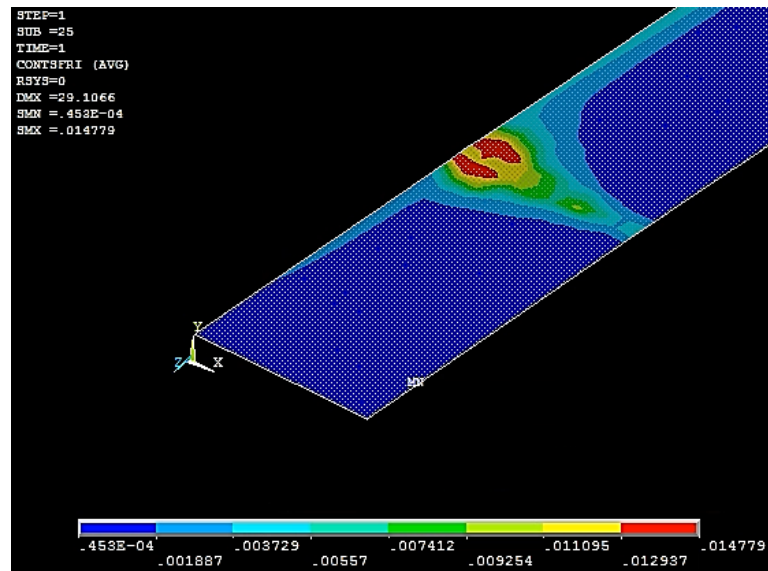


Figure 5.28: Sector B) GFRP – CFRP Adhesive Shear Stress Distribution Contour Plot (Araldite 2015)

Figure 5.29 compares the stress concentration along the external edge of the adhesive bondline between GFRP and CFRP detected in Araldite AV138 versus those detected in Araldite 2015. Due to brittle behavior of Araldite AV138 stresses

induced near the supports are higher than those induced in Araldite 2015. Figure 5.30 illustrates shear stresses in the adhesive between GFRP and CFRP are decreasing in lateral direction towards the interior of the adhesive bondline.

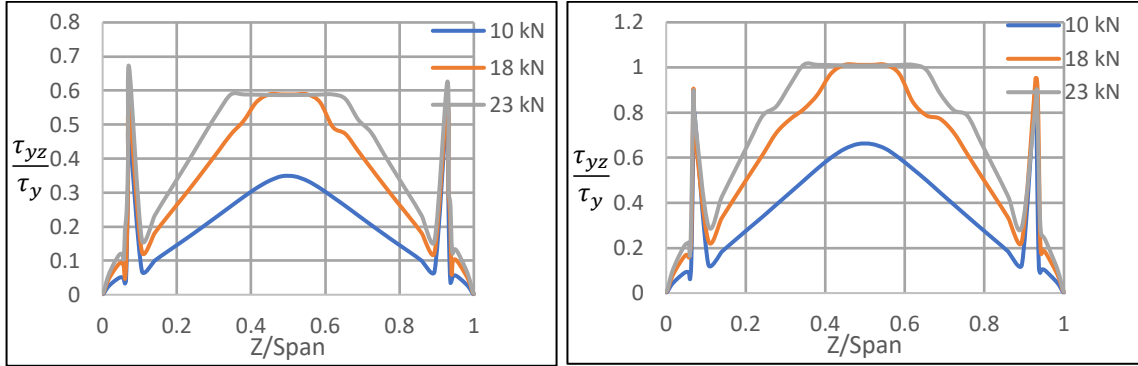


Figure 5.29: GFRP – CFRP Adhesive Longitudinal Shear Stress Distribution Plot Araldite AV 138 (left) vs Araldite 2015 (right)

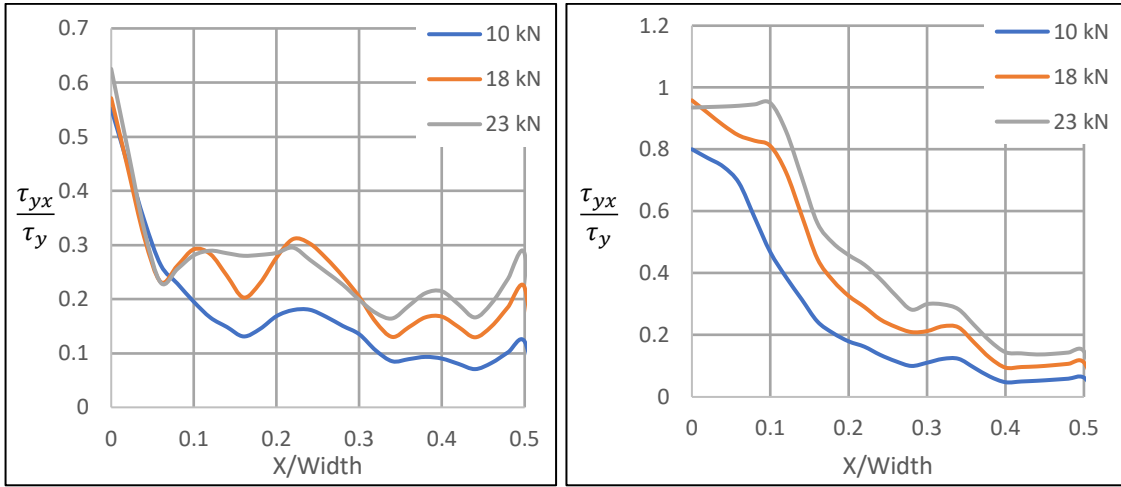


Figure 5.30: GFRP – CFRP Adhesive Lateral Shear Stress Distribution Plot Above the Left Support Araldite AV 138 (left) vs Araldite 2015 (right)

Figure 5.31 shows Araldite 2015 3-D normal stress distribution between GFRP and CFRP materials of the hybrid-composite unit. Similar normal stress distribution was observed for Araldite AV 138. The high normal stress concentrations were detected along the external edge of the overlap only. Similar, to the shear stresses,

extremes of the normal stress concentrations are localized near the supports. However, in this case this situation it is due to the low thickness of CFRP layer. The CFRP layer is so thin that most of the vertical force from the reactions is transmitted to the adhesive bondline. Normal stresses are decreasing in lateral direction towards the interior of the adhesive layer (see Figure 5.32).

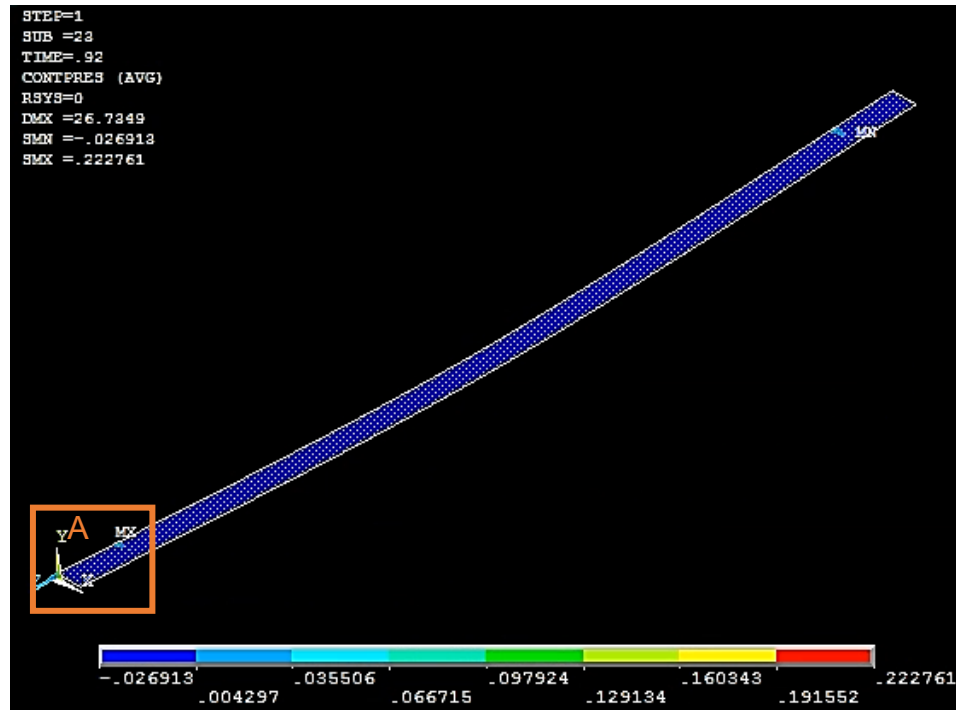


Figure 5.31: GFRP – CFRP Adhesive Normal Stress Distribution Contour Plot (Araldite 2015)

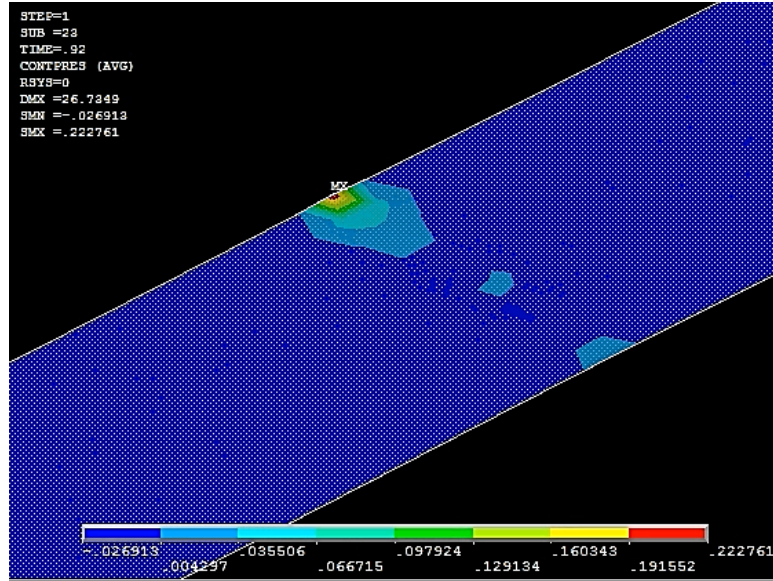


Figure 5.32: Sector A) GFRP – CFRP Adhesive Normal Stress Distribution Contour Plot (Araldite 2015)

Figure 5.33 compares normal stress concentration at GFRP-CFRP interface induced in two different Araldite epoxies. Almost no difference was found between the two stress distributions. However, both distributions have shown extremely high stress concentrations at the supports. This is most likely due to very small thickness of CFRP layer. Figure 5.34 illustrates that normal stresses, similar to the shear stresses, at the supports are decreasing in lateral direction towards the interior of the adhesive bondline.

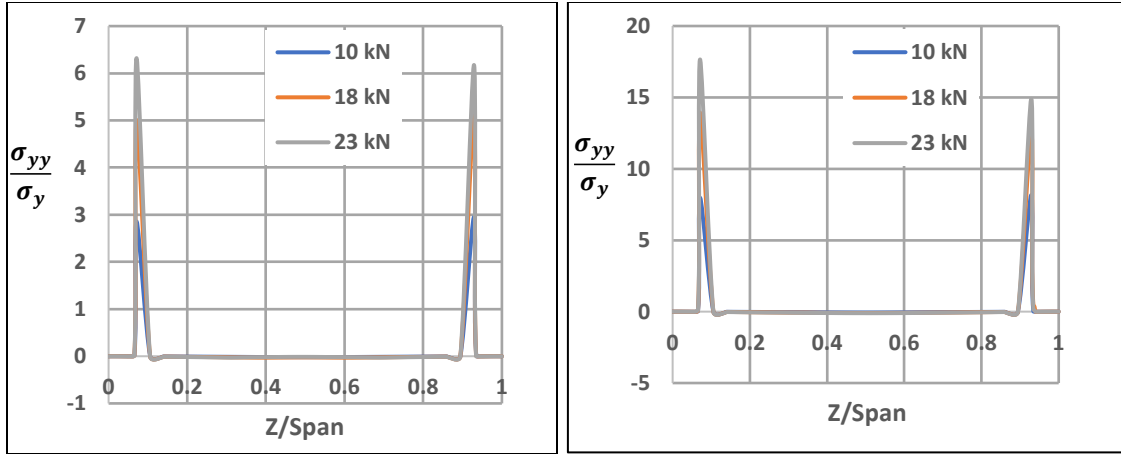


Figure 5.33: GFRP – CFRP Adhesive Longitudinal Normal Stress Distribution Plot Araldite AV 138 (left) vs Araldite 2015 (right)

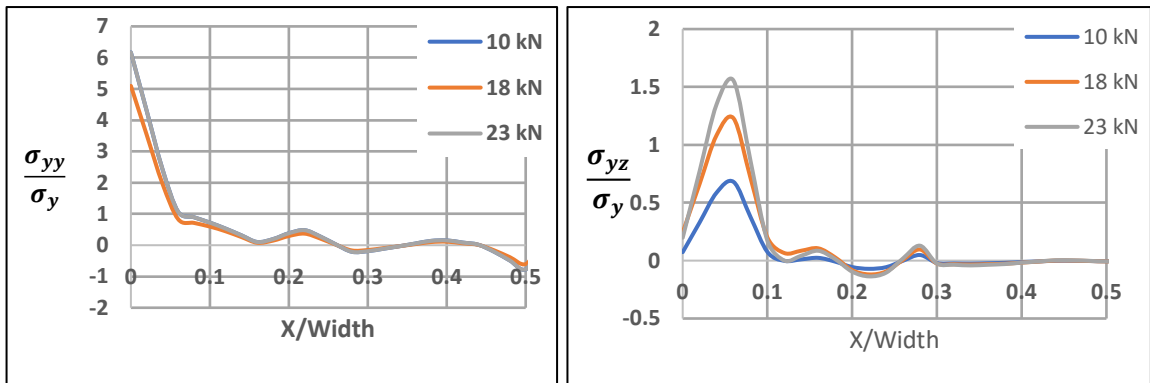


Figure 5.34: GFRP – CFRP Adhesive Lateral Normal Stress Distribution Plot Araldite at the Support AV 138 (left) vs Araldite 2015 (right)

The results of the FE contact analysis, using mix-mode CZM, predicted that the adhesive failure is most likely to occur in GFRP-CFRP interface prior to Concrete-GFRP interface. This prediction was based on quadratic nominal stress criterion (see (4.2)). Figure 5.35 and Figure 5.36 illustrate this assessment of damage initiation of both interfaces considering both adhesives. Per Figure 5.35, both adhesives in concrete-GFRP interface have not failed and remain elastic after full load was applied. Furthermore, when Araldite 2015 was modeled in concrete-

GFRP interface, the observed rate of stress development was greater than that of Araldite AV138 in the same interface. This can be explained by lesser Young's Modulus of Araldite 2015. Thus, Araldite 2015 is more ductile than Araldite AV 138.

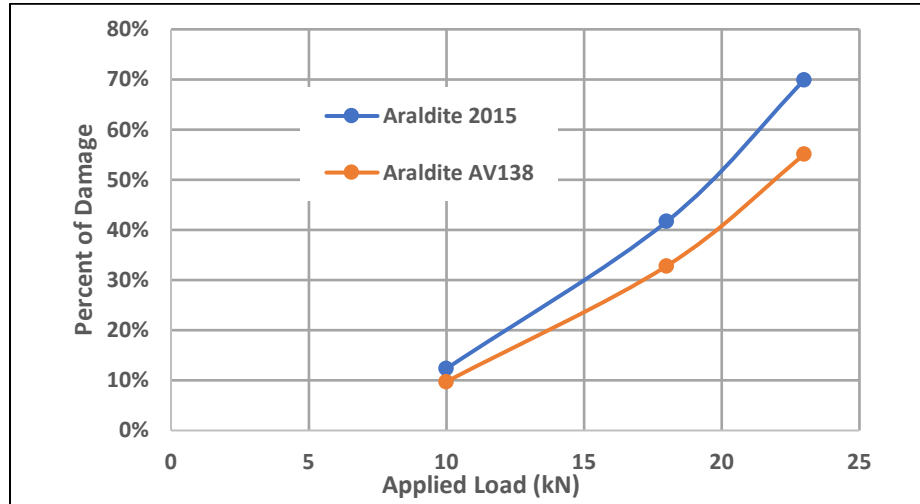


Figure 5.35: Concrete-GFRP Adhesive Bond Damage Initiation

The same pattern was observed in GFRP-CFRP interface considering both adhesives (see Figure 5.36). Per Figure 5.36, both adhesives exhibit elastic deformation after 4 kN was applied. Thus, through the remainder of the FE contact analysis, both adhesives in GFRP-CFRP interface exhibit plastic deformation.

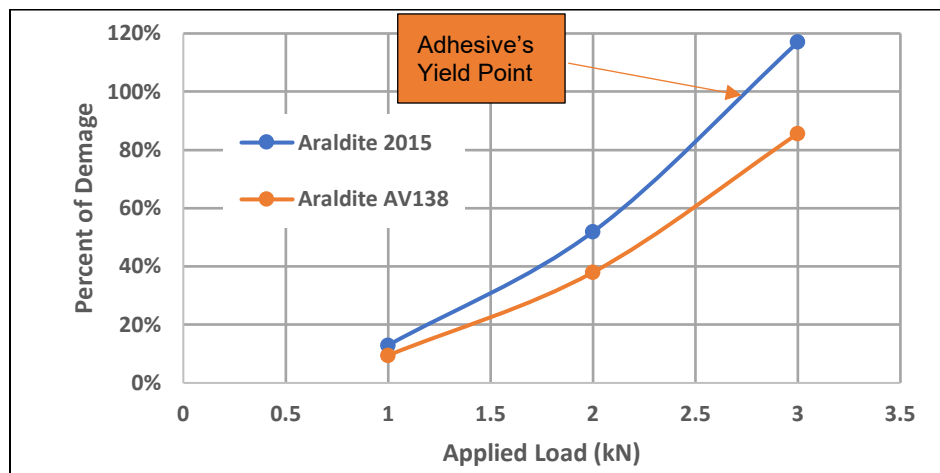


Figure 5.36: GFRP-CFRP Adhesive Bond Damage Initiation

Energy release rate of both adhesives was evaluated using the linear power law ((4.3). This law is used to assess plastic behavior of an adhesive after yielding and prior to the complete separation. The assessment illustrated in Figure 5.37, confirms predictions that ductile adhesives are more resilient to complete separation. The yielding of the Araldite 2015 has occurred prior to the brittle adhesive Araldite AV 138. Yet, the plastic deformation capacity of the more ductile Araldite 2015 was found to be much greater than Araldite AV 138. Therefore, Araldite 2015 did not undergo complete separation, as in the case of Araldite AV 138 (see Figure 5.37). For an applied load of 25 kN, Araldite 2015 showed a released energy of about 60% prior to the complete separation.

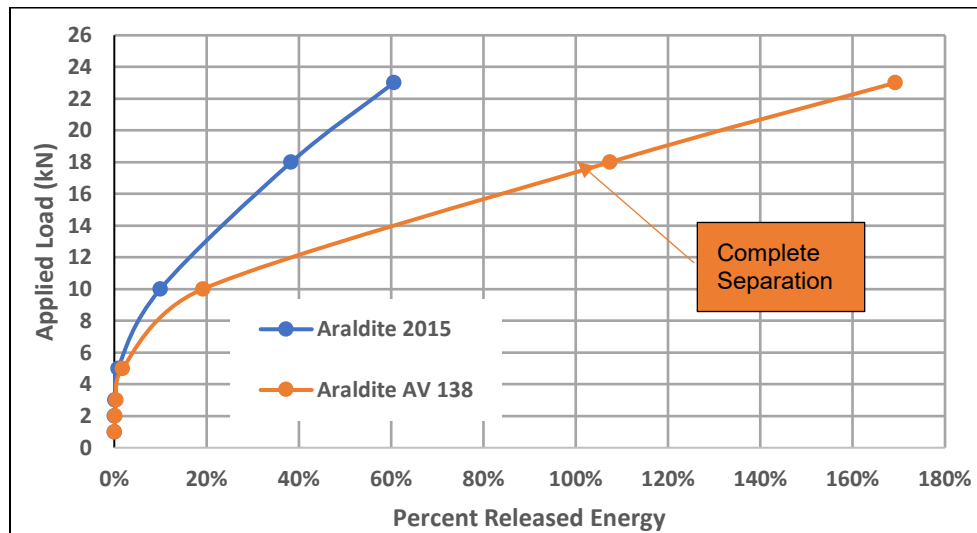


Figure 5.37: GFRP-CFRP Overall Percent of Strain Energy Released Rate

6 CONCLUSIONS AND RECOMMENDATIONS

The present study reviewed the current applications of adhesives and FRP materials in civil engineering. One of the discussed applications, is the hybrid-composite unit that was developed by Deskovic et al. (1995). This unit utilizes advantages of adhesive bonding as well as FRP materials. The unit showed good correlation between theory and results (Deskovic & Triantafillou, 1995). However, during laboratory tests adhesive bond had failed, and mechanical fasteners were added to complete the tests (Deskovic & Triantafillou, 1995). The use of only adhesive bonding without mechanical fasteners must be studied because of the great potential of the hybrid-composite unit application in civil engineering construction.

The numerical model used in the present study was validated by matching the results of the laboratory test reported by Deskovic et al. (1995). The numerical model predicts accurately the failure loads, displacements, and deformations of the hybrid-composite unit reported by Deskovic et al. (1995).

The investigation of cohesive failure was carried out using a 3-D finite element analysis with mix-mode cohesive zone material models. The study compared stresses induced in two structural adhesives, which are Araldite AV 138 and Araldite 2015.

The cohesive failure analysis revealed a complex 3-D state of stress for both adhesives. The stresses vary along the exterior of the bondline, besides their

variations in lateral direction. Highest stress concentrations were observed at the edges of the bondline. The normal stresses were controlling the failure in both adhesives bonding: concrete, GFRP, and CFRP. The present study concluded that higher joint strength is expected when ductile adhesive is used.

Future studies could be conducted to investigate the following:

- The bond strength between dissimilar materials of the hybrid-composite unit through physical three-point bending tests focusing on areas of high stress concentrations presented in this study.
- The bond strength between dissimilar materials of the hybrid-composite unit, using combination of ductile and brittle adhesives, through physical three-point bending tests. The brittle adhesive can be applied in the areas above the supports and at the center of the span, whereas ductile adhesive can be applied over remainder surface.
- Crack onset and growth in adhesives with finite thickness using the extended finite element method (XFEM).

REFERENCES

- Alkbrdaji, T. (2015). Strengthening of Concrete Structures Using FRP Composites. *Structure Magazine* , 18-20.
- American Society of Civil Engineers. (2017). *Infrastructure Report Card 2017*. American Society of Civil Engineers.
- ANSYS Inc. (2017). ANSYS Documentation. Sharcnet. Retrieved from https://www.sharcnet.ca/Software/Ansys/16.2.3/en-us/help/ai_sinfo/ans_intro.html
- ANSYS Inc. (2017, February 8). ANSYS Mechanical APDL Element Reference.
- Barbero, E. J. (2014). *Finite Element Analysis of Composite Materials Using ANSYS*. Boca Raton : CRC Press.
- Campilho, R., Banea, M., Neto, J., & da Silva, L. (2013). Modeling Adhesive Joints With Cohesive Zone Models: Effects of The Cohesive Law Shape of The Adhesive Layer. *International Journal of Adhesion and Adhesives*, 48-56.
- Campilho, R., Banea, M., Pinto, A., da Silva, L., & de Jesus, A. (2011). Strength Prediction of Single- and Double-Lap Joints by Standard and Extended Finite Element Modeling. *International Journal of Adhesion & Adhesives*, 363-372.
- Campilho, R., Moura, M. d., & J.J.M.S., D. (2008). Using a Cohesive Damage Model to Predict the Tensile Behaviour of CFRP Single-Strup Repairs. *International Journal Solid Structures*, 1497-1512.

- Carvalho, U., & Campilho, R. (2017). Validation of Pure Tensile and Shear Cohesive Laws Obtained by the Direct Method with Single-Lap Joints. *International Journal of Adhesion and Adhesives*, 41-50.
- Cook, R. D., & Young, W. C. (1999). *Advanced Mechanics of Materials*. New Jersey: Pearson.
- Da Silva, L., & Campilho, R. (2012). *Advances in Numerical Modeling of Adhesive Joints*. Springer.
- Deskovic, N., & Triantafillou, T. (1995). Innovative Design of FRP Combined with Concrete: Short-Term Behavior. *Journal Structural Engineering*, 1069-1078.
- G. Van Erp, T. H. (2002). *An Australian Approach to Fibre Composite Bridges*. Toowoomba Australia: FCDD, University of Southern Queensland.
- Grant, L., Adams, R., & da Silva, L. F. (2010). Experimental and Numerical Analysis of Single-Lap Joints for the Automotive Industry. *International Journal of Adhesion & Adhesives*, 405-413.
- Halliwell. (2000). *Polymer Composites in Construction*. London, UK: Construction Research Communications Ltd.
- He, X. (2011). A Review of Finite Element Analysis of Adhesively Bonded Joints. *Internaltional Journal of Adhesion & Adhesives*, 248-264.
- Hillman Composite Beam. (2011, June 1). Knickerbicker Bridge. Boothbay Harbor.
- Joannes, S., & Renard, J. (2009). Abaqus User Element for an Accurate Modeling of Adhesive Joints on Coarse Meshes. *SIMULIA Customer Conference*, (pp. 1-15).

- Jonathaan DePlanche, C. D. (2003). *New Oregon Road Bridge Replacenet* . Erie County Department of Public Works.
- Kadam, M. S., Firake , P., & Pawar, K. K. (2015). Finite Element Analysis of Single Lap Adhesive Joint Using RADIOSS. *Journal of Mechanical and Civil Engineering* , 66-76.
- Keller, T., Theodorou, N., Vassilopoulos, A., & de Castro, J. (2015). Effect of Natural Weathering on Durability of Pultruded Glass Fiber–Reinforced Bridge and Building Structures. *Composite Construction*.
- Korta, J., Andrzej, M., Zdziebko, P., & Uhl, T. (2014). Finite Element Analysis of Adhesive Bonds Using The Cohesive Zone Modeling Method. *Mechanics and Control*, 33(2), 51-57.
- Kumar, S., & Pandey, P. C. (2010). Behaviour of Bi-adhesive Joints. *Adhesion Science and Technology*, 1251-1281.
- O'Connor, J. S. (2008). Rapid Repscement of a Short Span Bridge Using a Pre-fabricated Lightweight Superstructure. *US-Taiwan Bridge Engineering Workshop* (p. Paper 09). New Jercey: Princeton.
- Queensland Goverment Department of Main Roads. (2006). *Fiber Composite Projects Technical Note 54*.
- Thompson, M. K., & Thompson, J. M. (2017). *ANSYS Mechanical APDL for Finite Element Analysis*. Elsevier Inc.
- Timoshenko, S., & Goodier, N. (1951). *Theory of Elasticity*. New York, Toronto, London: McGraw-Hill Book Company, Inc.

Waseem, M. H., & Kumar, K. N. (2014). Finite Element Modeling for Delamination Analysis of Double Cantiliver Beam Specimen. *International Journal of Mechanical Engineering*, 27-33.